6-24-2019

Dextral, normal, and sinistral faulting across the eastern California shear zone-Mina deflection transition, California-Nevada, USA

Kevin DeLano
Central Washington University

Jeffrey Lee
Central Washington University

Rachelle Roper
Central Washington University

Andrew Calvert
United States Geological Survey, Menlo Park

Recommended Citation

DeLano, K., Lee, J., Roper, R., and Calvert, A., 2019, Dextral, normal, and sinistral faulting across the eastern California shear zone–Mina deflection transition, California-Nevada, USA: Geosphere, v. 15, no. 4, p. 1206–1239, https://doi.org/10.1130/GES01636.1.

Research Paper

GEOSPHERE

GEOSPHERE, v. 15, no. 4

https://doi.org/10.1130/GES01636.1

15 figures; 4 tables; 1 set of supplemental files

CORRESPONDENCE: jeff@geology.cwu.edu

CITATION: DeLano, K., Lee, J., Roper, R., and Calvert, A., 2019, Dextral, normal, and sinistral faulting across the eastern California shear zone–Mina deflection transition, California-Nevada, USA: Geosphere, v. 15, no. 4, p. 1206–1239, https://doi.org/10.1130/GES01636.1.

Science Editor: Shanaka de Silva
Associate Editor: Terry L. Pavlis

Received 12 November 2017
Revision received 13 February 2019
Accepted 23 April 2019

Published online 24 June 2019

Dextral, normal, and sinistral faulting across the eastern California shear zone–Mina deflection transition, California-Nevada, USA

Kevin DeLano[1,*], Jeffrey Lee[1], Rachelle Roper[1,†], and Andrew Calvert[2]

[1]Department of Geological Sciences, Central Washington University, Ellensburg, Washington 98926, USA
[2]U.S. Geological Survey, Menlo Park, California 94025, USA

ABSTRACT

Strike-slip faults commonly include extensional and contractional bends and stepovers, whereas rotational stepovers are less common. The Volcanic Tableland, Black Mountain, and River Spring areas (California and Nevada, USA) (hereafter referred to as the VBR region) straddle the transition from the dominantly NW-striking dextral faults that define the northwestern part of the eastern California shear zone into a rotational stepover characterized by dominantly NE-striking sinistral faults that define the southwestern Mina deflection. New detailed geologic mapping, structural studies, and $^{40}Ar/^{39}Ar$ geochronology across the VBR region allow us to calculate Pliocene to Pleistocene fault slip rates and test predictions for the kinematics of fault slip transfer into this rotational stepover. In the VBR, Mesozoic basement is nonconformably overlain by a Miocene sequence of rhyolite, dacite, and andesite volcanic rocks that yield $^{40}Ar/^{39}Ar$ ages between 22.878 ± 0.051 Ma and 11.399 ± 0.041 Ma. Miocene rocks are unconformably overlain by an extensive sequence of Pliocene basalt and andesite lava flows and cinder cones that yield $^{40}Ar/^{39}Ar$ ages between 3.606 ± 0.060 Ma and 2.996 ± 0.027 Ma. The Pliocene sequence is, in turn, unconformably overlain by Quaternary tuffs and sedimentary rocks. This sequence of rocks is cut by NS- to NW-striking normal faults across the Volcanic Tableland that transition northward into NS-striking normal faults across the Black Mountain area and that, in turn, transition northward into NW-striking dextral and NE-striking sinistral faults in the River Spring area. A range of geologic markers were used to measure offset across the faults in the VBR, and combined with the age of the markers, yield minimum ~EW-extension rates of ~0.5 mm/yr across the Volcanic Tableland and Black Mountain regions, and minimum NW-dextral slip and NE-sinistral slip rates of ~0.7 and ~0.3 mm/yr, respectively, across the River Spring region. In the River Spring area, our preferred minimum dextral slip and sinistral slip rates are 0.8–0.9 mm/yr and 0.7–0.9 mm/yr, respectively. We propose three kinematic fault slip models, two irrotational and one rotational, whereby the VBR region transfers a portion of dextral Owens Valley fault slip northwestward into the Mina deflection. In irrotational model 1, Owens Valley fault slip is partitioned into two components, one northeastward onto the White Mountain fault zone and one northwestward into the Volcanic Tableland. Slip from the two zones is then transferred northward into the southwestern Mina deflection. In irrotational model 2, Owens Valley fault slip is partitioned into three components, with the third component partitioned west-northwest onto the Sierra Nevada frontal fault zone. In the rotational model, predicted sinistral slip rates across the southwestern Mina deflection are at least 115% greater than our observed minimum slip rates, implying our minimum observed rates underestimate true sinistral slip rates. A comparison of summed geologic fault slip rates, parallel to motion of the Sierra Nevada block relative to the central Great Basin, from the Sierra Nevada northeastward across the VBR region and into western Nevada are the same as geodetic rates, if our assumptions about the geologic slip rate across the dextral White Mountain fault zone is correct.

INTRODUCTION

Strike-slip fault zones commonly include bends whereby the fault is continuous through the bend defining either a zone of divergence (a releasing or extensional bend) or a zone of convergence (a constraining or contractional bend) (e.g., Crowell, 1974; Christie-Blick and Biddle, 1985; Gamond, 1987). Strike-slip fault zones also define stepovers which are characterized by either releasing (extensional) or restraining (contractional) slip transfer between overlapping, but distinct subparallel strike-slip faults (e.g., Wilcox et al., 1973; Crowell, 1974; Aydin and Nur, 1982; Cunningham and Mann, 2007). Geologic structures observed in releasing bends or stepovers include normal faults, pull-apart basins, extensional strike-slip duplexes, and transtensional relay ramps and structures observed in restraining bends or stepovers include thrust faults, push-up ridges, positive flower structures, and contractional strike-slip duplexes (e.g., Cunningham and Mann, 2007).

Stepovers defined by rotating fault-bounded rigid blocks, or transrotational deformation (e.g., Ingersoll, 1988; Dickinson, 1996) (Fig. 1A), are less commonly observed. In rotational stepovers, blocks rotate in the direction of shear imposed across the zone between the distinct subparallel strike-slip faults. As a consequence, the faults bounding the rotating blocks record strike-slip motion in a direction opposite that of slip along the bounding overlapping strike-slip faults (McKenzie and Jackson, 1983, 1986; Dickinson, 1996) (Fig. 1A). If the ends of the rotating blocks are pinned to the bounding overlapping strike-slip faults and maintain constant length, the width between the bounding overlapping

*Now at Instream Flow Unit, Division of Water Rights, State Water Resources Control Board, Sacramento, California 95814, USA
†Now at Pioneer Natural Resources, 5205 N. O'Conner Blvd #200, Irving, Texas 75039, USA

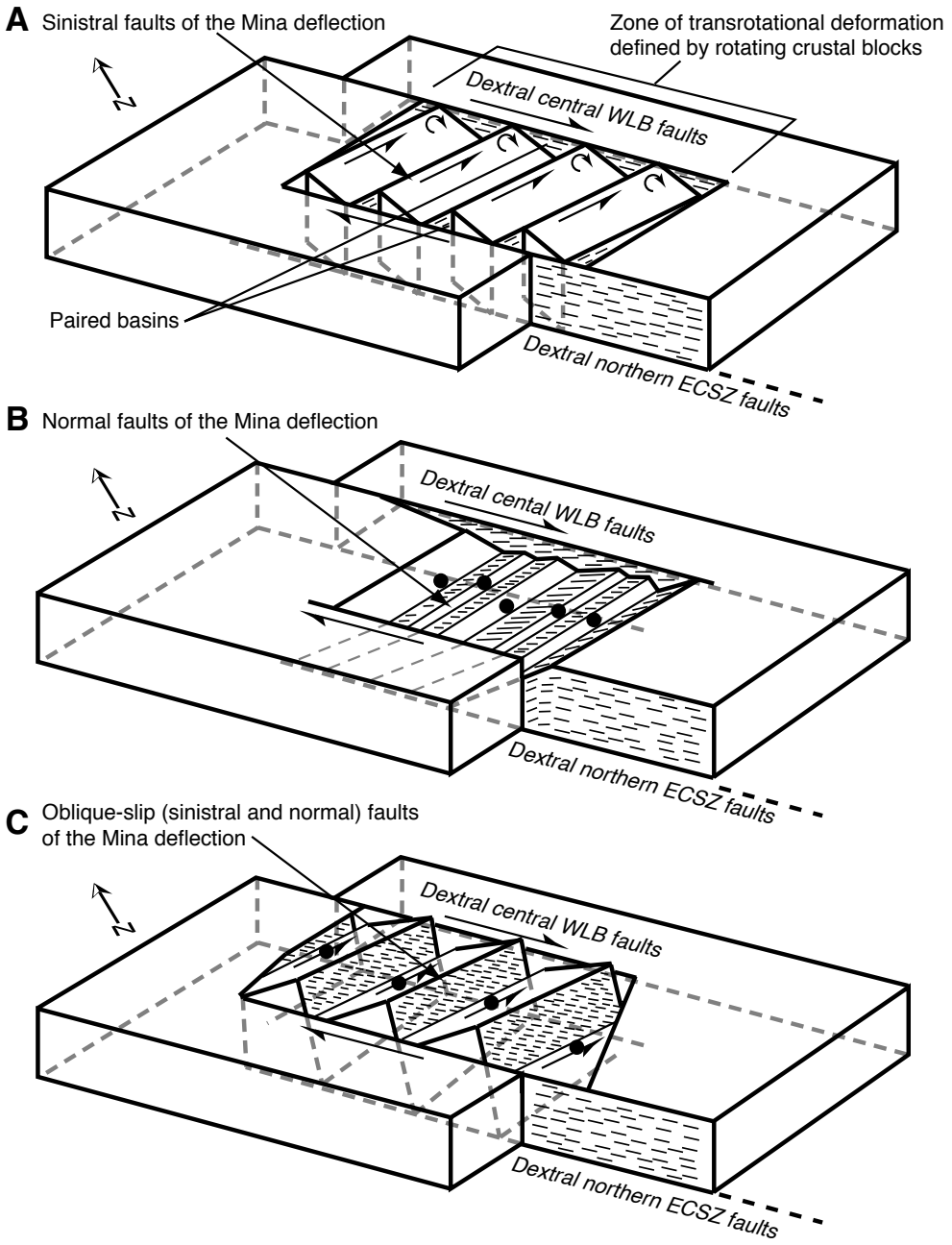

Figure 1. Block models illustrating the different fault types proposed to accommodate fault slip across the Mina deflection, a right stepover within the dextral eastern California shear zone (ECSZ)–Walker Lane belt (WLB), California-Nevada, USA. (A) The clockwise block rotation model in which sinistral slip bounding clockwise rotating rigid blocks transfers fault slip (modified from McKenzie and Jackson, 1983, 1986; Wesnousky, 2005). (B) The displacement-transfer model whereby an extensional stepover, defined by normal faults, transfers slip across the stepover (modified from Oldow, 1992; Oldow et al., 1994). (C) The transtensional model whereby a combination of sinistral and normal slip along connecting faults transfers slip across the stepover. Single-barbed arrows show dextral fault motion across faults of the ECSZ-WLB and sinistral motion along faults in the Mina deflection; half-circle double-barbed arrows indicate clockwise rotating fault blocks; solid ball is located on the hanging wall of normal slip faults; thin short lines indicate slip direction on fault surfaces.

strike-slip faults will increase (transtension) and then decrease (transpression) as the blocks rotate (McKenzie and Jackson, 1983, 1986; Dickinson, 1996). Alternatively, if the shear zone and rotating blocks maintain constant width, then the ends of the rotating blocks will undergo contraction and then extension during rotation (Dickinson, 1996). The net slip across a rotational stepover can be greater than the sum of offsets along the faults bounding the rotating blocks. Thus, fault kinematic reconstructions that assume irrotational deformation in strike-slip fault systems that bound rotating rigid blocks will likely fall short of a complete fault kinematic evolution model and of assessment of net slip (Dickinson, 1996).

The eastern California shear zone (ECSZ)–Walker Lane Belt (WLB), a ~130–75-km-wide zone of NW-dextral shear located in eastern California and western Nevada, USA (Fig. 2), exposes extensional stepovers, such as the Deep Springs normal fault (Lee et al., 2001) and similarly oriented normal faults to the southeast (Fig. 1B), and stepover zones of clockwise rotating blocks bounded by sinistral faults in the Carson domain (Cashman and Fontaine, 2000) and the Mina deflection (Wesnousky, 2005; Petronis et al., 2009; Nagorsen-Rinke et al., 2013; Bormann et al., 2016) (Fig. 1B). In the Carson domain, Cashman and Fontaine (2000) used paleomagnetic data to propose a kinematic model that includes translation, clockwise rotation of rigid blocks accommodated by sinistral slip on faults bounding the blocks, and extension. In the Mina deflection stepover, three kinematic models have been proposed to accommodate fault slip transfer across this zone. (1) Wesnousky's (2005) observations on the geometry, sinistral offset, and paired basins at the ends of active faults across the Mina deflection support a model of NE-trending fault blocks, bounded by sinistral faults, rotating clockwise within a broad zone of NW-striking dextral shear (Fig. 1A). Nagorsen-Rinke et al. (2013) reached the same conclusion based on observations on the geometry and sinistral offset of Pliocene faults in the southwestern Mina deflection. Paleomagnetic data, indicating ~5–60° of clockwise rotation since the middle Miocene, across the Mina deflection also supports this interpretation (Petronis et al., 2009; Rood et al., 2011; Grondin et al., 2016). (2) Geologic map, structural, and seismic data from across the Mina deflection region underpinned Oldow's (1992) and Oldow et al.'s (1994) displacement-transfer model, whereby normal faults transfer slip (a releasing stepover) (Fig. 1B). (3) Based on GPS velocity, earthquake focal mechanism, and fault-slip inversion data sets, Oldow (2003) proposed a transtensional model whereby both normal and sinistral slip occurred on faults within the stepover (Fig. 1C). In Oldow's (2003) model, deformation in the western Mina deflection is characterized by extension-dominated transtension and deformation in the eastern part is characterized by wrench-dominated transtension.

To document the net dextral shear across a stepover zone of clockwise rotating blocks, one must characterize the geometric, structural, and kinematic evolution of the stepover zone (e.g., McKenzie and Jackson, 1983, 1986; Dickinson, 1996) and the zone of transition from dextral shear to clockwise rotation. To assess the mechanism by which the Mina deflection stepover zone developed, we describe the geometry and kinematics along structures within the Volcanic Tableland, Black Mountain, and River Spring areas (California and Nevada) (hereafter referred to as the VBR region) which defines the transition from the NW-dextral slip dominated northwestern ECSZ to the NE-sinistral slip dominated southwestern Mina deflection (Figs. 2 and 3). We revisit the Pleistocene horizontal extension deformation rates across the Volcanic Tableland (cf. Pinter, 1995), and use new geologic mapping, structural studies, and $^{40}Ar/^{39}Ar$ geochronology in the Black Mountain and River Spring areas (Fig. 3) to calculate Pliocene to Pleistocene horizontal extension, dextral, and sinistral fault slip rates across the VBR. These data, combined with published fault slip rates on other faults in this region (Stockli et al., 2000; Bradley, 2005; Kirby et al., 2006, 2008; Lee et al., 2006, 2009a; Tincher and Stockli, 20019; Nagorsen-Rinke et al., 2013), also allow us to refine the proposed kinematic model of Nagorsen-Rinke et al. (2013) for this transition zone, propose a simple transrotational model for the VBR region, and address the apparent discrepancy between short-term geodetic and long-term geologic slip rates across the northern part of the ECSZ.

REGIONAL TECTONIC SETTING

Geodetic and geologic studies indicate that dextral shear between the Pacific and North American plates is partitioned among the San Andreas fault system (~75%–80% of the plate motion) and the ECSZ-WLB (~25%–20% of the plate motion) (e.g., Dokka and Travis, 1990; Dixon et al., 1995, 2000; Bennett et al., 2003) (Fig. 2). Across the ECSZ-WLB, dextral shear is accommodated primarily along a set of NNW- to NW-striking dextral faults, which strike sub-parallel to Pacific-North America plate motion, and along a lesser set of ~NS-striking normal faults and ENE-striking sinistral faults (Figs. 2 and 3).

Dextral slip across the relatively narrow (~90 km wide) northwestern part of the ECSZ is concentrated on two major NW-striking dextral faults, the White Mountain fault zone and the Fish Lake Valley fault zone. These two fault zones transfer slip northward into the broad (~125 km long by ~45 km wide) ENE-trending, right-stepping Mina deflection (Figs. 2B and 3). Thus, the Mina deflection defines a stepover within the NW-trending dextral WLB-ECSZ and is composed of sinistral, dextral, and normal faults (Wesnousky, 2005; Bradley, 2005; Lee et al., 2006, 2009b; Tincher and Stockli, 2009; Nagorsen-Rinke et al., 2013; this study).

Approximately 175 km south of the Mina deflection stepover (at latitude of ~36.5°N) (Fig. 2B), summation of long-term (10^3–10^6 yrs) geologic fault slip rates along a transect perpendicular to Pacific-North America plate motion (i.e., 313°) (Dixon et al., 2000) across the ECSZ yields the same value within error, ~9.3 mm/yr, as geodetic (10^1 yrs) strain rates (c.f. Bennett et al., 2003; Lee et al., 2009a). In contrast, ~70 km south of the Mina deflection stepover (at latitude of ~37.5° N), the modeled far field geodetic strain rate, calculated parallel to motion of the Sierra Nevada block relative to the central Great Basin (SN-CGB; 323°) along transect A-A′ (Fig. 3), is 10.6 ± 0.5 mm/yr (Lifton et al., 2013). This GPS rate is 370%–170% greater than the summed late Pleistocene (10^4 yrs) geologic dextral fault slip rate of ~3.0–5.9 mm/yr (Frankel et al., 2011;

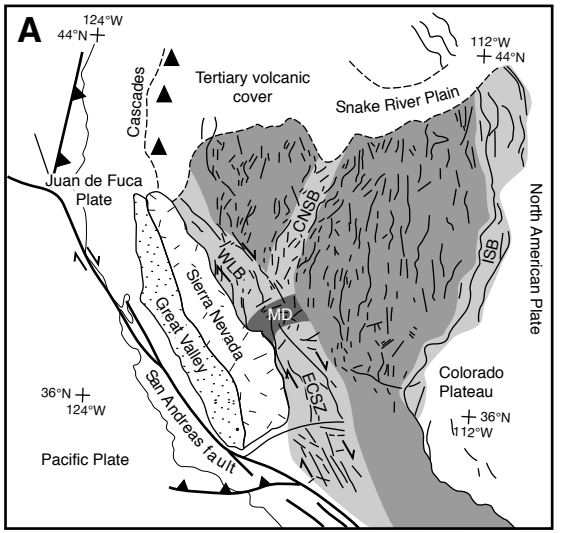

Figure 2. (A) Simplified tectonic map of the western U.S. Cordillera showing the modern plate boundaries and tectonic provinces. Basin and Range Province is in medium gray; CNSB (Central Nevada seismic belt), ECSZ (eastern California shear zone), ISB (intermountain seismic belt), and WLB (Walker Lane belt) are in light gray; MD (Mina deflection) is in dark gray. (B) Shaded relief map of the Walker Lane Belt and northern part of the eastern California shear zone showing the major Quaternary faults, the Carson domain, MD, and the Silver Peak–Lone Mountain extensional complex (SPLM). Light-blue squares show locations of GPS sites that bound the Mina deflection (Bormann et al., 2016); solid ball is located on the hanging wall of normal faults; arrow pairs indicate relative motion across strike-slip faults. AH—Anchorite Hills fault zone; BSF—Benton Springs fault; CF—Coaldale fault; CVF—Clayton Valley fault; DSF—Deep Springs fault; EPF—Emigrant Peak fault; EF—Excelsior fault; FCDV—Furnace Creek–Death Valley fault zone; FLVFC—Fish Lake Valley fault–Furnace Creek fault zone; GHF—Gumdrop Hills fault; HLF—Honey Lake fault; HMF—Hunter Mountain fault; LMF—Lone Mountain fault; MVF—Mohawk Valley fault; OVF—Owens Valley fault; PLF—Pyramid Lake fault; PSF—Petrified Springs fault; PVF—Panamint Valley fault; QVF—Queen Valley fault; RVF—Round Valley fault; SAF—San Antonio Mountains range front fault; SLF—Stateline fault; SNFF—Sierra Nevada frontal fault zone; TPF—Towne Pass fault; WMF—White Mountains fault zone; WRF—Wassuk Range fault; WSFZ—Warm Springs fault zone.

Figure 3's maps, labels, and data sets are organized in a series of layers that may be viewed separately or in combination using the capabilities of the Acrobat (PDF) layering function (click "Layers" icon along vertical bar on left side of window for display of available layers; turn layers on or off by clicking the box to the left of the layer name). To access the PDF of the figure, please visit https://doi.org/10.1130/GES01636.f3 or access the full-text article on www.gsapubs.org.

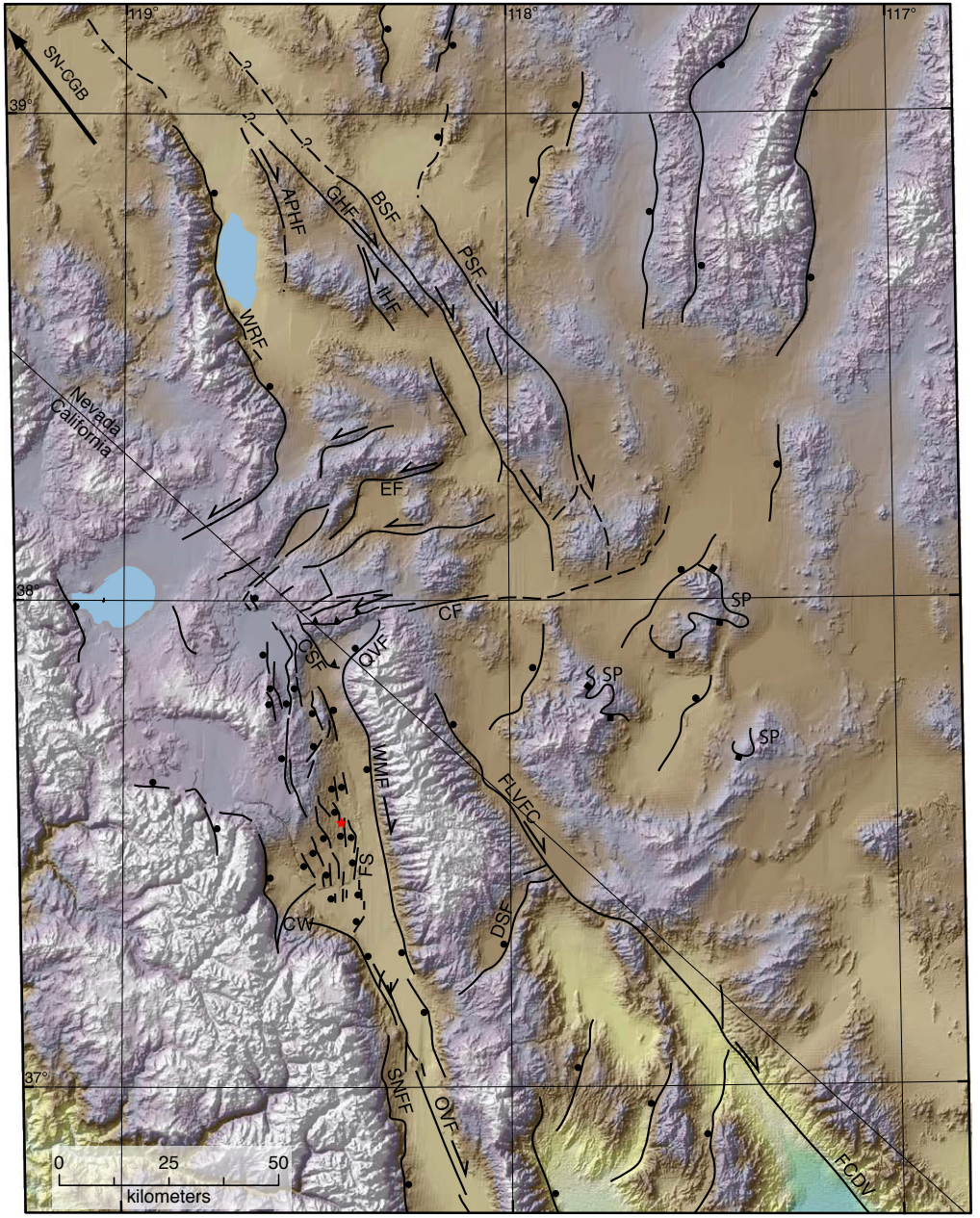

A. Shaded Relief Map and Faults | B. Geographic Names | C. Domain Names | D. Field Areas | E. GPS Vectors

Figure 3. Layer A: Shaded relief map showing major Quaternary faults across the western Basin and Range Province, central Walker Lane, Mina deflection, and northern eastern California shear zone, California-Nevada, USA. Heavy black arrow in the northwest corner of the map shows the present-day azimuth of motion of the Sierra Nevada block with respect to the central Great Basin (SN-CGB) (Bennett et al., 2003); red star marks the epicenter of the 1986 Ms 6.2 Chalfant Valley earthquake (Lienkaemper et al., 1987; Smith and Priestley, 2000). APHF—Agai Pai Hills fault; CSF—Coyote Springs fault; CW—Coyote Warp; EF—Excelsior fault; FCDV—Furnace Creek-Death Valley fault zone; FLVFC—Fish Lake Valley–Furnace Creek fault zone; FS—Fish Slough; IHF—Indian Head fault; SP—Silver Peak–Lone Mountain detachment fault (squares on the upper plate). Remaining abbreviations and fault symbols defined in Figure 2B. Base map modified from Faulds and Henry (2008). Layer B: Geographic names for major mountain ranges and valleys. Layer C: Structural domains of Basin and Range Province, central Walker Lane, Mina deflection, and northern eastern California shear zone. Layer D: Field study areas. Blue dashed polygons show field study areas where Pliocene to Quaternary geologic fault slip rates have been published or are field study areas referenced in the text; yellow dashed polygons show the locations of the Black Mountain and River Spring geologic maps (see Figs. 6A and 7A). Layer E: GPS velocities across the Basin and Range Province, central Walker Lane, Mina deflection, and northern eastern California shear zone. Thin blue arrows show GPS velocities relative to stable North America (ITRFNA2005 reference frame) from Lifton et al. (2013) and heavy multi-colored arrows show GPS velocities relative to stable North America (NA12 North America reference frame) from Bormann et al. (2016). GPS velocity scales are in the upper left corner of the map. Yellow line A-A′, which extends ~57 km southwest beyond the figure, marks the transect along which the modeled geodetic strain rate parallel to SN-CGB motion is 10.6 ± 0.5 mm/yr (Lifton et al., 2013). Maps, labels, and data sets are organized in a series of layers that may be viewed separately or in combination using the capabilities of the Acrobat (PDF) layering function (click "Layers" icon along vertical bar on left side of window for display of available layers; turn layers on or off by clicking the box to the left of the layer name). To access the PDF of the figure, please visit https://doi.org/10.1130/GES01636.f3 or access the full-text article on www.gsapubs.org.

Kirby et al., 2006; Reheis and Sawyer, 1997; Hoeft and Frankel, 2010; Foy et al., 2012; Lifton et al., 2013). Like the GPS rate, the geologic rate was calculated parallel to motion of the SN-CGB along transect A-A′ at the latitude of ~37.5°N (Fig. 3). The discrepancy between GPS and geologic slip rates imply: (1) the apparent "missing" geologic slip is accommodated by distributed dextral shear east of the Fish Lake Valley fault zone or west of the White Mountain fault zone (Frankel et al., 2007; Kirby et al., 2006; Lee et al., 2009b; Nagorsen-Rinke et al., 2013), (2) the unaccounted for slip is accommodated on active faults that cross transect A-A′ (Fig. 3), although the slip rates on these faults were not included in the summed slip rate of Lifton et al. (2013), (3) the region is experiencing a strain transient whereby the decadal time scale slip rate is recording a pulse in dextral shear deformation compared to the long-term geologic slip rate which records an average dextral shear rate over 10^3–10^6 yr (cf. Rockwell et al., 2000; Peltzer et al., 2001; Oskin et al., 2007; Pérouse and Wernicke, 2016), or (4) the discrepancy is not due to missing tectonic fault slip, but to additional present-day magmatic strain the consequence of dike injection or magma emplacement (e.g., Bursik and Sieh, 1989; Smith et al., 2004). In addition, the geodetic rate at the latitude of ~37.5°N is somewhat larger than the Bennett et al. (2003) estimate farther south. Lifton et al. (2013) suggested that the difference in geodetic rates was because the ~10.6 mm/yr rate included predicted interseismic strain accumulation beyond the distal data points of the A-A′ transect.

To address the discrepancy between geodetic and geologic slip rates, Nagorsen-Rinke et al. (2013) proposed a kinematic model whereby the unaccounted for geologic slip is, at least in part, accommodated along faults within a broad zone of dextral shear (Figs. 2B, 3, and 4). An additional motivating factor in developing this kinematic model was Nagorsen-Rinke et al.'s (2013) observation that the White Mountain fault zone could not transfer dextral slip to the sinistral faults in the Adobe Hills (Fig. 3). To address this issue, their kinematic model predicts that dextral slip along the NNW-striking Owens Valley fault is partitioned northward into two components (Fig. 4). The first component is defined by a northeast extensional stepover, via normal faults across the basin that underlies Bishop, California (Sheehan, 2007), onto the NNW-striking dextral White Mountain fault zone (Figs. 3 and 4). Dextral slip along the White Mountain fault zone, in turn, transfers slip northwestward into

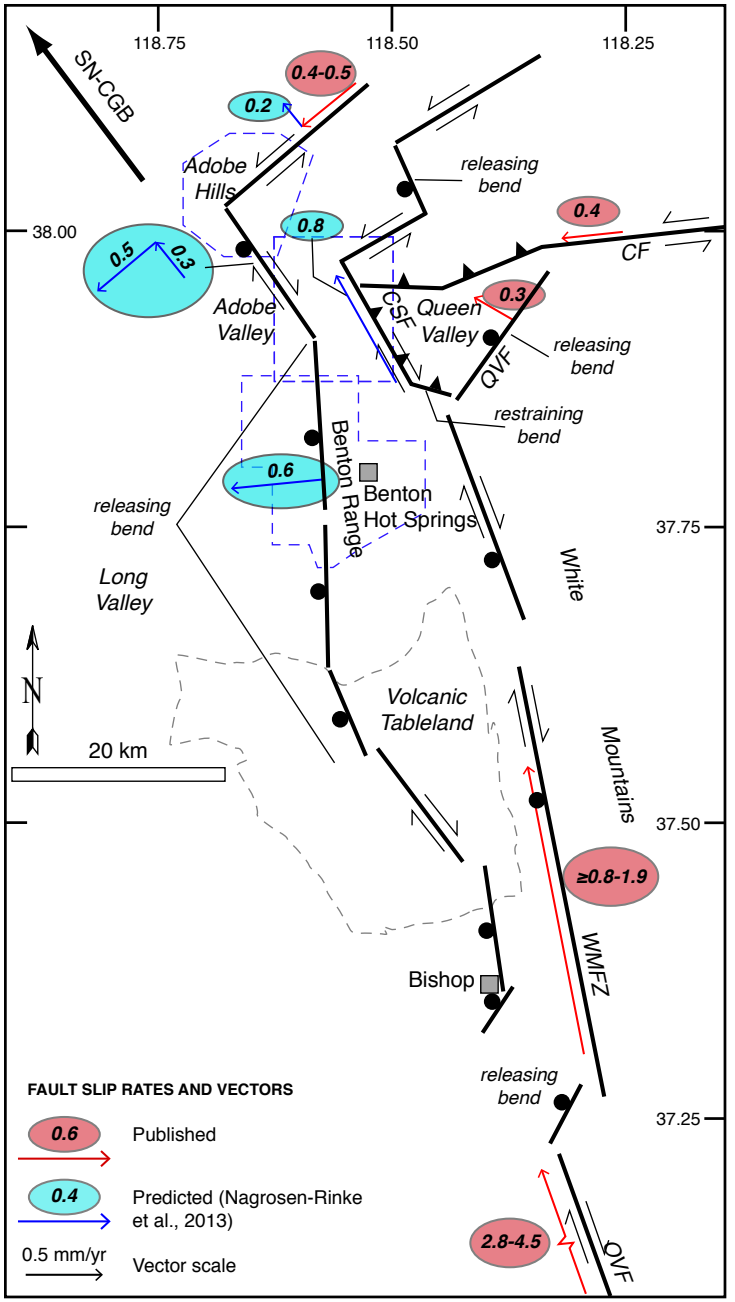

Figure 4. Fault slip kinematic model for the northwestern eastern California shear zone and southwestern Mina deflection, California–Nevada, USA (modified from Nagorsen-Rinke et al., 2013). Map shows a simplified version of major normal and dextral fault zones (cf. Fig. 3) that define the proposed kinematic link between dextral slip along the Owens Valley fault in the south with sinistral slip along faults in the southwestern Mina deflection, and the link between dextral fault slip along the White Mountain fault zone and normal, dextral, and thrust fault slip in the Queen Valley region. Blue dashed polygons show the location of map areas Black Mountain (south), River Spring (middle), and Adobe Hills (Nagorsen-Rinke et al., 2013) (north). Fault symbols defined in Figure 3; fault abbreviations are defined in Figures 2B and 3. Published fault slip rates are from: Adobe Hills (Nagorsen-Rinke et al., 2013); Coaldale fault (Bradley, 2005; Lee et al., 2006); Owens Valley fault (Kirby et al., 2006); Queen Valley fault (Stockli et al., 200; Lee et al., 2009b); White Mountain fault zone (Kirby et al., 2008; Lifton, 2013). See text for details.

the Queen Valley region of the Mina deflection; here dextral slip is partitioned into a right step onto the Queen Valley normal fault and a left step onto the dextral-thrust Coyote Springs fault (Lee et al., 2009b). The second component is defined by transfer of slip to the northwest via ~NS- to NW-striking normal faults in the Volcanic Tableland, which transfer slip northward onto ~NNW- to ~NS-striking normal faults in the Black Mountain area. Black Mountain area faults, in turn, transfer slip onto NW-striking dextral-normal oblique faults in the River Spring area, which abut ENE-striking sinistral faults in the Adobe Hills region of the southwestern Mina deflection (Figs. 3 and 4).

Nagorsen-Rinke et al.'s (2013) kinematic model and Lee et al.'s (2009b) kinematic model across the Queen Valley region (Fig. 4) use published fault slip rates along the sinistral Coaldale fault (Bradley, 2005; Lee et al., 2006; Tincher and Stockli, 2009), the Queen Valley normal fault (Lee et al., 2009a; Tincher and Stockli, 2009; Stockli et al., 2000), dextral and sinistral faults in the Adobe Hills region (Nagorsen-Rinke et al., 2013), the dextral White Mountain fault zone (Kirby et al., 2006), and the northern end of the dextral Owens Valley fault (Kirby et al., 2008) to make slip rate predictions for several faults across the ECSZ–Mina deflection transition including 0.6 mm/yr of ENE-WSW–extension across the Black Mountain area, and 1.1 mm/yr of NW-dextral shear and 0.5 mm/yr of NE-SW extension across the River Spring area (Fig. 4). This model provided a kinematic link between sinistral faults in the southwestern Mina deflection and the dextral Owens Valley fault and reduced—but did not eliminate—the discrepancy between geologic and geodetic rates (Nagorsen-Rinke et al., 2013). In this paper, we test the Nagorsen-Rinke et al. (2013) model's inferred deformation style and rate across the Volcanic Tableland and predicted deformation styles and rates across two regions, the Black Mountain and River Spring regions (Fig. 4). We revisit the horizontal extension deformation rates across the Volcanic Tableland (cf. Pinter, 1995), and based on new geologic mapping, structural studies, and $^{40}Ar/^{39}Ar$ geochronology in the Black Mountain and River Spring areas (Fig. 3), calculate Pliocene to Pleistocene horizontal extension, dextral, and sinistral fault slip rates across the northern part of the VBR. These data also allow us to address the discrepancy between short-term geodetic and long-term geologic slip rates across the northern part of the ECSZ.

GEOLOGIC SETTING OF THE VBR REGION

The VBR covers an ~800 km^2 region located across the transition from northwestern part of the ECSZ to the southwestern part of the Mina deflection between the White Mountains to the east and Long Valley caldera and the Sierra Nevada to the west (Fig. 3). The VBR is underlain by Paleozoic and Mesozoic metasedimentary and metavolcanic rocks, Mesozoic volcanic and intrusive rocks, Neogene and Quaternary volcanic, volcaniclastic, and sedimentary rocks, and normal, dextral, and sinistral faults (Rinehart and Ross, 1957; Bateman, 1965; Gilbert et al., 1968; Crowder and Sheridan, 1972; Crowder et al., 1972; Krauskopf and Bateman, 1977; Oldow, 1992; Reheis et al., 2002; Bradley, 2005; Lee et al., 2006, 2009b; Tincher and Stockli, 2009; Petronis et al., 2009; Oldow et al., 2009; Nagorsen-Rinke et al., 2013; this study).

In the northwestern ECSZ, the NW-striking dextral Fish Lake Valley fault zone strikes subparallel to the 323° direction of SN-CGB motion (Bennett et al., 2003), and the NNW-striking dextral Owens Valley fault–White Mountain fault zone strikes ~20–25° clockwise with respect to the direction of SN-CGB motion (Fig. 3). The NNW-strike of the present-day Owens Valley fault–White Mountain fault zone is hypothesized to record reactivation of a major dextral shear zone of Laramide age (Late Cretaceous–early Paleogene) (Bartley et al., 2007). NE- to EW-striking sinistral faults define the Mina deflection (e.g., Bradley, 2005; Lee et al., 2006; Wesnousky, 2005; Tincher and Stockli, 2009; Nagorsen-Rinke et al., 2013; this study). The geometry of these faults is interpreted as inherited from pre-Cenozoic geology and structure including Paleozoic and Mesozoic contractional structures, which in turn follow the trend of an embayment in the early Paleozoic rifted continental margin of the western U.S. (Oldow et al., 1989, 2009; Tosdal et al., 2000).

Two episodes of Neogene deformation have been documented across the northwestern ECSZ–southwestern Mina deflection: (1) Mid-Miocene E-W extensional deformation resulting in tilting and normal offset of pre-Cenozoic rocks and Miocene ignimbrite and basalt lava flows and (2) Pliocene to present-day deformation characterized by a combination of sinistral, dextral, and normal faulting (Gilbert et al., 1968; Lienkaemper et al., 1987, Stockli et al., 2000, 2003; Bradley, 2005; Lee et al., 2006, 2009b; Tincher and Stockli, 2009; Nagorsen-Rinke et al., 2013; this study).

The southern VRB includes the Volcanic Tableland which is defined by the geomorphic surface of the Bishop Tuff, a rhyolitic pyroclastic flow ejected south and east into the Owens Valley during the eruption of Long Valley caldera at 766.6 ± 3.1 ka (Gilbert, 1938; Bailey et al., 1976; Chamberlain et al., 2014). The normal faults that cut the tuff dominantly strike ~N-S (Bateman, 1965; Pinter, 1995) (Fig. 3).

In the central VBR is the Black Mountain area (Fig. 3), which is underlain by Neogene to Quaternary tuffs, lava flows, gravel deposits, and alluvium unconformably overlying Mesozoic intrusive rocks. All rock units but the youngest Quaternary sedimentary deposits are cut by ~NS- to NNW-striking, W-dipping normal faults (Krauskopf and Bateman, 1977; this study).

The River Spring area, located in the northern part of the VBR, is underlain by Neogene to Quaternary lavas, debris flows, an ignimbrite, cinder cones, and alluvial and wind-blown sedimentary deposits (Gilbert et al., 1968; Krauskopf and Bateman, 1977; this study) (Fig. 3). In the southern River Spring area, NW-striking dextral faults dominate, whereas in the northern part of the River Spring area NE-striking sinistral faults dominate. Thus, the River Spring area straddles the boundary between the NW-striking dextral faults that define the northwestern part of the ECSZ and NE-striking sinistral faults that define the southwestern Mina deflection.

The largest recorded earthquake in the VBR was the 1986 M_s 6.2 Chalfant Valley earthquake sequence in the northeastern Volcanic Tableland (Fig. 3), which along with smaller earthquakes throughout the area (http://www.ncedc

.org/recenteqs/) indicates that faults in the VBR are seismically active. The 1986 surface rupture propagated to the southeast, through the Chalfant Valley, and onto an ~11-km-long segment of the White Mountain fault zone (Fig. 3) (Lienkaemper et al., 1987). Smith and Priestly (2000) used aftershock hypocenters to interpret a NW-striking, SW-dipping strike-slip fault in Chalfant Valley and suggested this structure transfers dextral slip from the White Mountain fault zone northwest to the Volcanic Tableland.

ROCK UNITS AND AGES IN THE VBR

Rock units in the VBR area consist of Mesozoic basement, Miocene and Pliocene sequences dominated by volcanic rocks, and a Quaternary sequence of volcanic and sedimentary rocks. The basement of Mesozoic plutonic rocks is nonconformably overlain by Miocene rhyolite tuffs, andesite lava flows, andesite lava flow breccias, and stream deposits. The Miocene units are overlain, in angular unconformity, by Pliocene basalt and andesite lava flows, cinder cones, and stream deposits. Pliocene rocks, in turn, are overlain in angular unconformity by Quaternary rhyolite tuffs, and alluvial, fluvial, eolian, colluvial, playa, and landslide deposits (Rinehart and Ross, 1957; Bateman, 1965; Crowder et al., 1972; Crowder and Sheridan, 1972; Krauskopf and Bateman, 1977; this study) (Figs. 5, 6, and 7). Below we briefly describe the rock units exposed in the VBR area, and their ages. Detailed unit descriptions are provided in Figure 5, $^{40}Ar/^{39}Ar$ ages are summarized in Table 1, and a description of our $^{40}Ar/^{39}Ar$ analytical techniques, and supporting age spectra and probability density plots of ages are provided in the Supplemental File[1].

The oldest rock unit, Mesozoic plutonic basement (unit TRJg) associated with the Sierra Nevada batholith (Krauskopf and Bateman, 1977), is exposed within the Black Mountain area and southern part of the River Spring area (Figs. 5, 6, and 7). Unit Mrt (sanidine $^{40}Ar/^{39}Ar$ age of 22.878 ± 0.051 Ma; Table 1) is a rhyolite tuff that nonconformably overlies unit TRJg and is widespread across the northeastern part of the Black Mountain area (Figs. 5 and 6). Miocene andesite lava flows and lava flow breccia, units Map and Mab, respectively, overlie unit Mrt.

The oldest Cenozoic units exposed in the River Spring area are Miocene andesite lava flows, unit Maf (Gilbert et al., 1968; Krauskopf and Bateman, 1977; this study) (Figs. 5 and 7). Unit Maf is overlain by Miocene dacite lava flows, debris flows, and dikes, and a pumice-rich deposit (units Mdh, Mdf, and Mp) which are exposed only along the upper reaches of the Pizona Creek region (Figs. 5 and 7). One of the dacite flows yields an $^{40}Ar/^{39}Ar$ age of 14.695 ± 0.816 Ma on groundmass plagioclase (Table 1). The youngest Miocene unit in the River Spring area is a welded ignimbrite, unit Mlt, also exposed in the Pizona Creek region. In the adjacent Adobe Hills, Nagorsen-Rinke et al. (2013) reported an $^{40}Ar/^{39}Ar$ age of 11.399 ± 0.041 Ma on plagioclase for this welded ignimbrite (this sample age is recalculated using a revised age of 28.4378 Ma for the Taylor Creek sanidine standard [Fleck and Calvert, 2016] so that the age is comparable to astronomical age of Kuiper et al. [2008]). Locally overlying the Miocene volcanic rocks in the Black Mountain and River Spring areas are thin gravel deposits and a tuffaceous sandstone (units MPg, Pg, and Pts) (Figs. 5, 6, and 7).

Interfingered Pliocene basalt and andesite lavas overlie unit TRJg, Miocene volcanic units, and Miocene–Pliocene sedimentary units. These lavas are areally extensive in the northeast and southern part of the Black Mountain area, and are the most aerially extensive rock types in the River Spring area (Figs. 5, 6, and 7). Inconsistent stratigraphic relationships between flows and overlapping $^{40}Ar/^{39}Ar$ ages across the Adobe Hills, Black Mountain, Huntoon Springs, and River Spring areas suggest that these Pliocene lava flows interfinger (Nagorsen-Rinke et al., 2013; Hogan, 2014; this study) (Figs. 3, 5, 6, and 7). $^{40}Ar/^{39}Ar$ geochronology on groundmass plagioclase from these flows indicate they range in age from 3.606 ± 0.060 Ma to 3.348 ± 0.027 Ma (Nagorsen-Rinke et al., 2013; Hogan, 2014; this study) (Table 1). Cinder deposits (unit Pvc), which define seven volcanic centers, and basalt scoria deposits (unit Pbs) overlie the basalt and andesite lavas (Figs. 5, 6, and 7). One of the volcanic centers in the west-central part of the River Spring area is cut by a set of radiating basalt dikes, one of which yields a groundmass plagioclase $^{40}Ar/^{39}Ar$ age of 2.996 ± 0.063 Ma (Table 1). The dikes were likely emplaced synchronously with the development of the volcanic center, and thus we interpret their age as the age of development of the volcanic center.

Quaternary tuffs are exposed only in the Black Mountain area and overlie, in nonconformity, unit TRJg and in an angular unconformity on Miocene–Pliocene rocks (Figs. 5 and 6). The oldest Quaternary tuff is the Benton Stream tuff, unit Qbst, which outcrops northwest of the Benton Hot Springs (Figs. 5 and 6). The Tuff of Taylor Canyon, unit Qtc (sanidine $^{40}Ar/^{39}Ar$ age of 1.976 ± 0.013 Ma; Table 1) drapes the eastern flanks of the Benton Range and Black Mountain. Based on its eruption age, we correlate unit Qtc to ca. 1.9 Ma explosive eruptions from the Glass Mountain volcano, which is located along the northeast margin of Long Valley caldera ~5 km west of the Black Mountain map area (Fig. 3) (Krauskopf and Bateman, 1977; Metz and Mahood, 1985). The Bishop Tuff, unit Qbt (zircon $^{206}Pb/^{238}U$ age of 766.6 ± 3.1 ka; Chamberlain et al., 2014), is exposed on the eastern flank of Blind Springs Hill, California (Figs. 5 and 6) (Crowder et al., 1972; this study) and defines the Volcanic Tableland (Rinehart and Ross, 1957; Bateman, 1965; Crowder and Sheridan, 1972). Quaternary sedimentary rocks exposed in the VBR consist of older and younger alluvium; colluvium, alluvial fan, landslide, playa, and fluvial terrace deposits; and eolian tuffaceous sand (see Figs. 6A and 7A for unit labels).

NEOGENE–QUATERNARY FAULTING IN THE VBR

To document the style, geometry, magnitude of deformation, and relative timing of faulting across the VBR, we revisited the fault geometries across the Volcanic Tableland, and completed new detailed mapping and structural studies of the Black Mountain and River Spring areas (Figs. 6, 7, and 8). Geochronology on key volcanic units allows us to determine the timing of faulting

Supplemental File
$^{40}Ar/^{39}Ar$ Geochronology

To document the timing of volcanism and faulting, and to calculate fault slip rates across the VBR, 14 samples collected from the Miocene, Pliocene, and Quaternary volcanic sequence were dated using $^{40}Ar/^{39}Ar$ incremental heating techniques or with a continuous CO_2 laser system following the methods described in Nagorsen-Rinke et al. (2013) and Dalrymple and Duffield (1988) (Figs. S1, S2, and S3). $^{40}Ar/^{39}Ar$ geochronology samples were prepared and analyzed following the procedures outlined in Supplemental File 1 in Nagorsen-Rinke et al. (2013). Clean separates (either groundmass plagioclase or sanidine), collected from one rhyolite tuff (Mrt), one hornblende dacite (Mdh), five basalt flows (Pbp_2, Pbb, Pbc, Pbm_1, and Pbm_2), two andesite flows (Pah and Pa), one dike from one of the volcanic centers (Pvc), and the Tuff of Taylor Canyon (Qtc), yield either plateau ages, a decreasing age spectra, a result of ^{39}Ar recoil (Turner and Cadogan, 1974; Onstott et al., 1995), or weighted mean ages (Figs. S1, S2, and S3). For samples affected by ^{39}Ar recoil, the recoil model age is calculated by incorporating age dispersion into the weighted mean age error (e.g. Nagorsen-Rinke et al., 2013).

The Miocene units, Mrt and Mdh, yield a sanidine weighted mean age and a groundmass model recoil age of 22.878 ± 0.051 Ma and 14.695 ± 0.816 Ma, respectively (Fig. S1). Groundmass plagioclase from the five basalt flow units (Pbb, Pbm_1, Pbm_2, Pbc, and Pbp_2) and two andesite flow units (Pah and Pa) yield plateau ages or model recoil ages that range between 3.606 ± 0.060 Ma to 3.361 ± 0.020 Ma (Fig. S2); and groundmass plagioclase from a basaltic dike cross-cutting one of the Pvc cones yields a model recoil age of 2.996 ± 0.063 Ma (Fig. 2). Our geochronologic data suggest that the Pliocene mafic volcanism across the Black Mountain-River Spring area occurred over a relatively short time span of ~550 ka, similar to the Adobe Hills region (Nagorsen-Rinke et al., 2013). Sanidine from the Tuff of Taylor Canyon (unit Qtc) yields a weighted mean age of 1.976 ± 0.013 Ma (Fig. S3).

References Cited

Dalrymple, G.B., and Duffield, W.A., 1988, High precision $^{40}Ar/^{39}Ar$ dating of Oligocene rhyolites from the Mogollon-Datil volcanic field using a continuous laser system: Geophysical Research Letters, v. 15, p. 366–463.
Nagorsen-Rinke, S., Lee, J., and Calvert, A., 2013, Pliocene sinistral slip across the Adobe Hills, eastern California–western Nevada: Kinematics of fault slip transfer across the Mina

[1]Supplemental File. Supplemental file provides a description of our $^{40}Ar/^{39}Ar$ analytical techniques, and includes supporting age spectra and probability density plots of ages. Please visit https://doi.org/10.1130/GES01636.S1 or access the full-text article on www.gsapubs.org to view the Supplemental File.

Composite Stratigraphic Column for the Black Mountain and River Spring areas

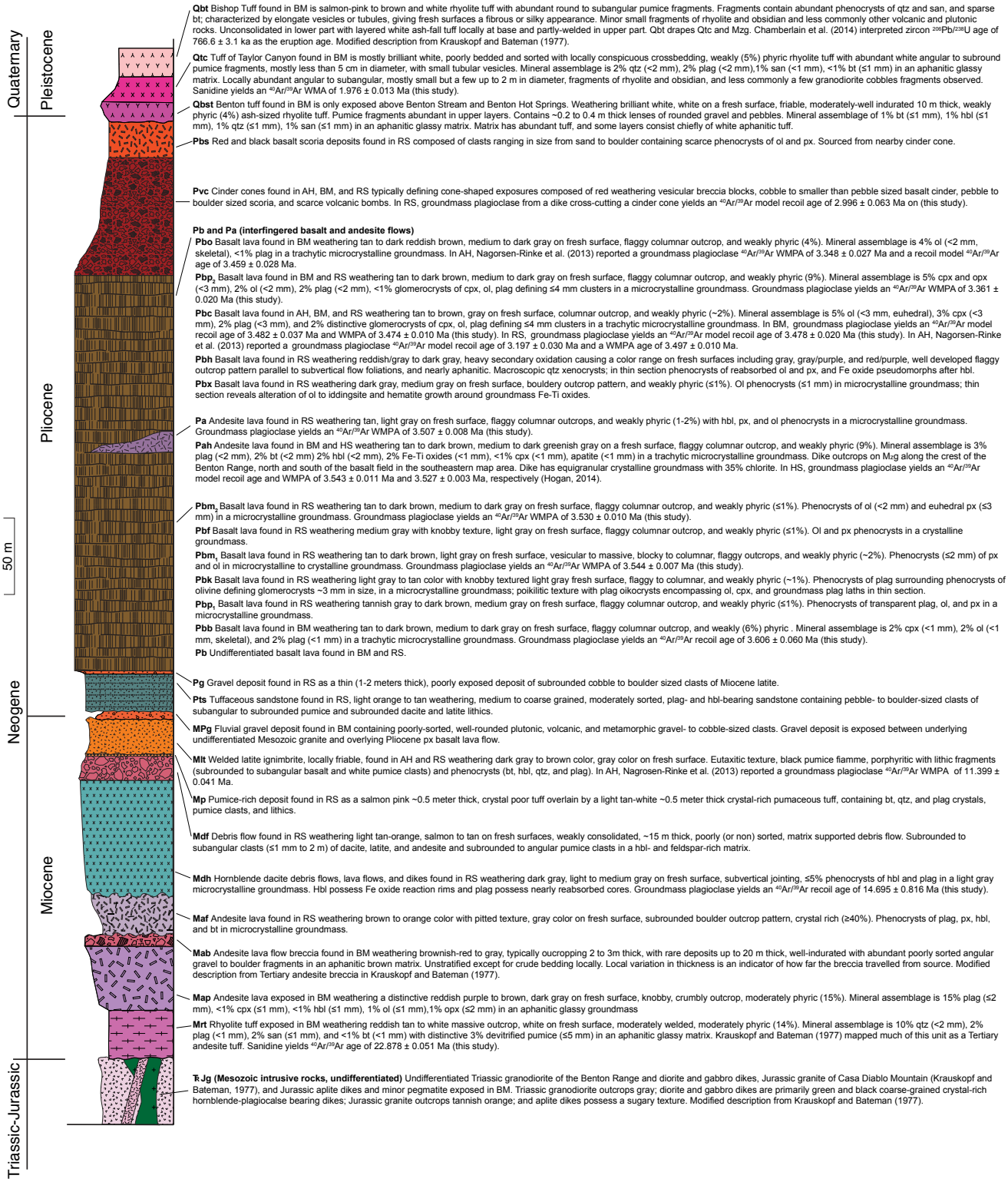

Figure 5. Composite stratigraphic column of Mesozoic igneous basement, Miocene, Pliocene, and early to middle Pleistocene volcanic and sedimentary rocks exposed in the Black Mountain and River Spring areas, California-Nevada, USA. Relative thicknesses are shown. Field area abbreviations (see Fig. 3 for locations): AH—Adobe Hills; BM—Black Mountain; HS—Huntoon Spring; RS—River Spring area. Mineral abbreviations: bt—biotite; cpx—clinopyroxene; hbl—hornblende; ol—olivine; opx—orthopyroxene; plag—plagioclase feldspar; px—undifferentiated pyroxene; qtz—quartz; san—sanidine. Other abbreviations: WMPA—weighted mean plateau age; WMA—weighted mean age. Sample $^{40}Ar/^{39}Ar$ ages from Nagorsen-Rinke et al. (2013) are recalculated using a revised age of 28.7348 Ma for the Taylor Creek sanidine standard (Fleck and Calvert, 2016) so that the age is comparable to the astronomical age of Kuiper et al. (2008).

Figure 6A is intended to be viewed at a width of 29 in. To view at full size, please visit https://doi.org/10.1130/GES01636.f6a or access the full-text article on www.gsapubs.org.

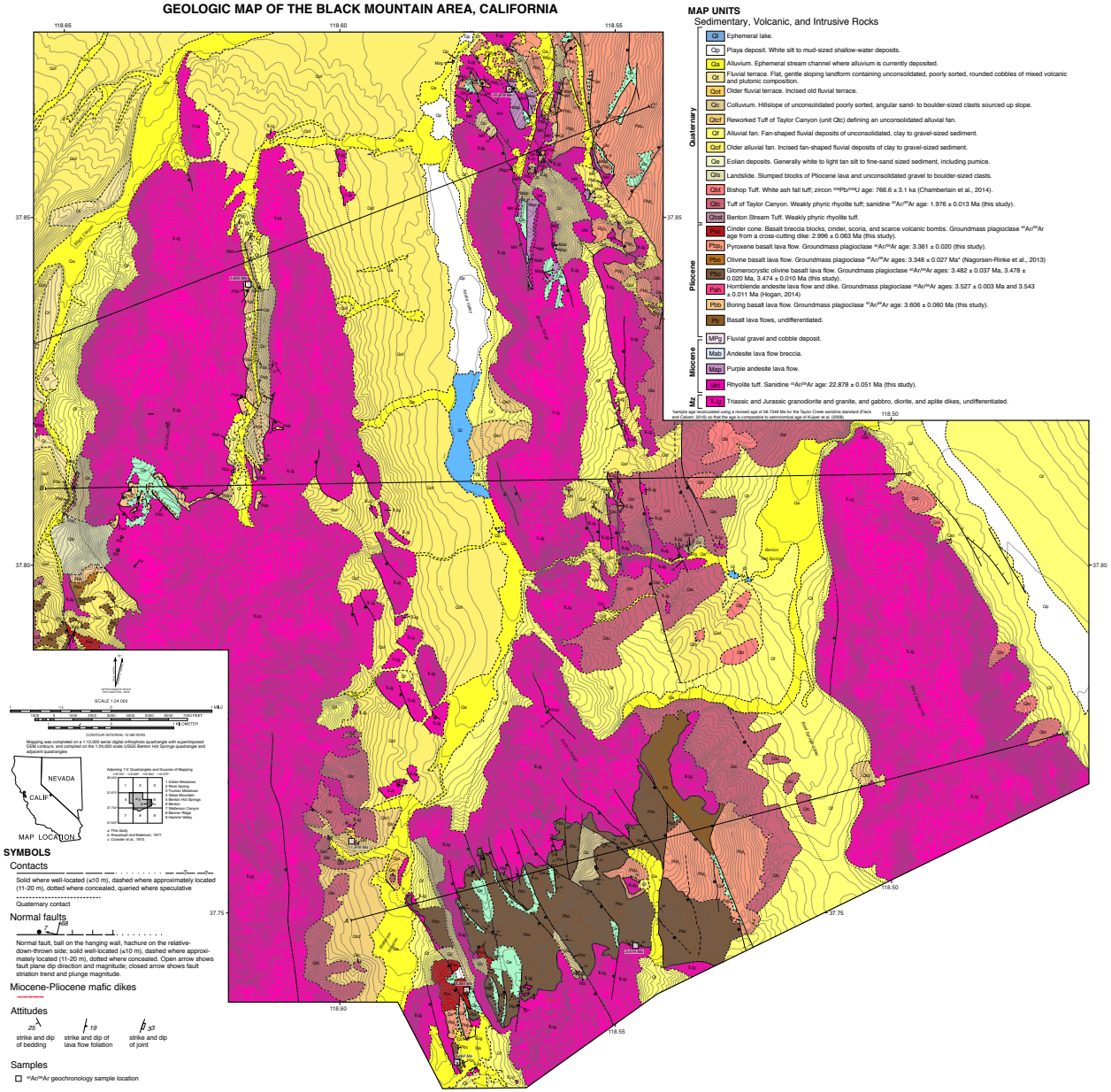

Figure 6. (A) Geologic map of the Black Mountain area California, USA (1:24,000 scale). See Figure 3 for location. Figure 6A is intended to be viewed at a width of 29 in. To view at full size, please visit https://doi.org/10.1130/GES01636.f6a or access the full-text article on www.gsapubs.org. (*Continued on following page.*)

Figure 6B is intended to be viewed at a width of 25 in. To view at full size, please visit https://doi.org/10.1130/GES01636.f6b or access the full-text article on www.gsapubs.org.

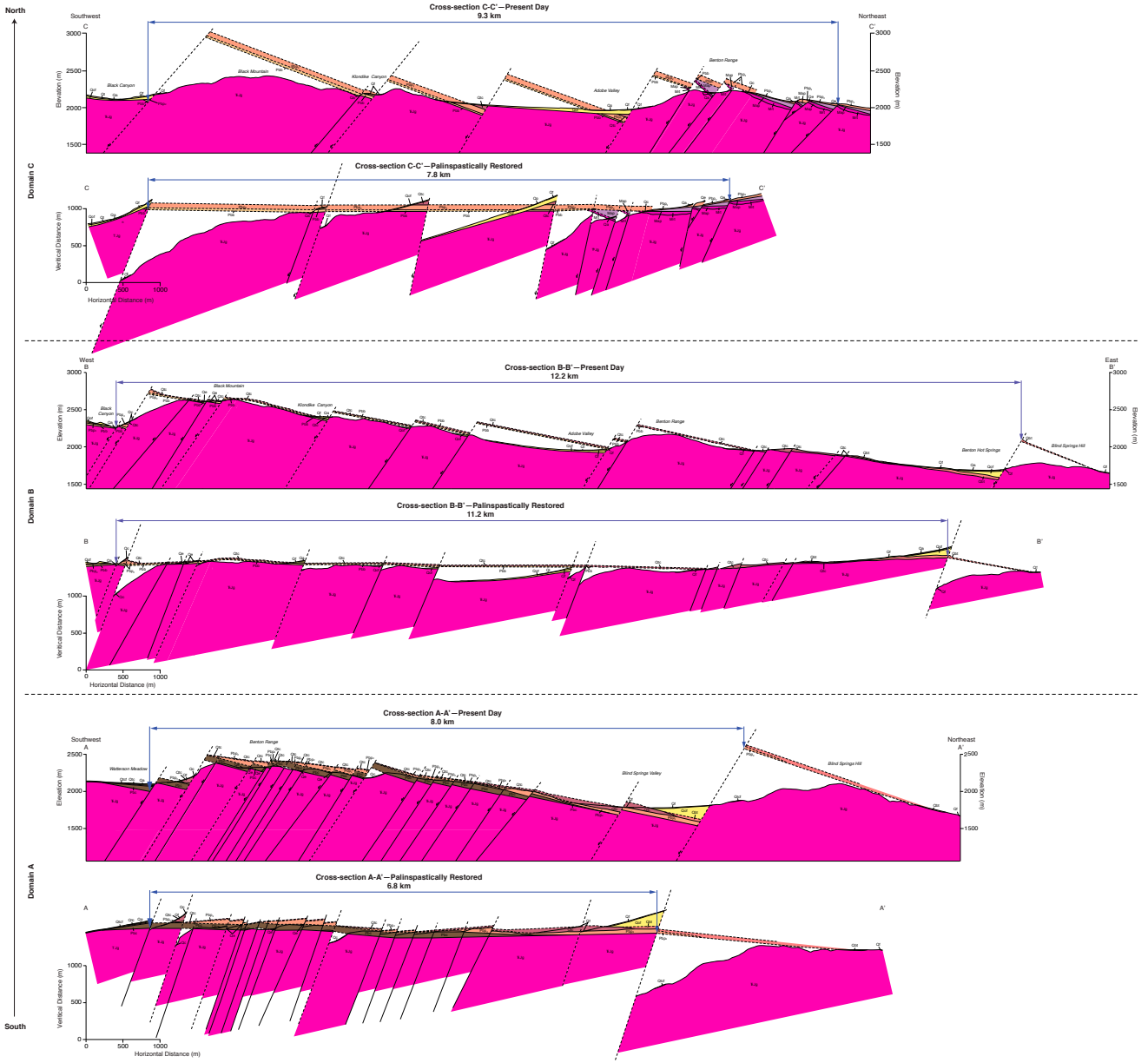

Figure 6 (*continued*). (B) Interpretative northwest-southeast and east-west present-day and palinspastically restored geologic cross-sections across the Black Mountain area. DEM—digital elevation model; USGS—U.S. Geological Survey. Figure 6B is intended to be viewed at a width of 25 in. To view at full size, please visit https://doi.org/10.1130/GES01636.f6b or access the full-text article on www.gsapubs.org.

Figure 7A is intended to be viewed at a width of 20.1 in. To view at full size, please visit https://doi.org/10.1130/GES01636.f7a or access the full-text article on www.gsapubs.org.

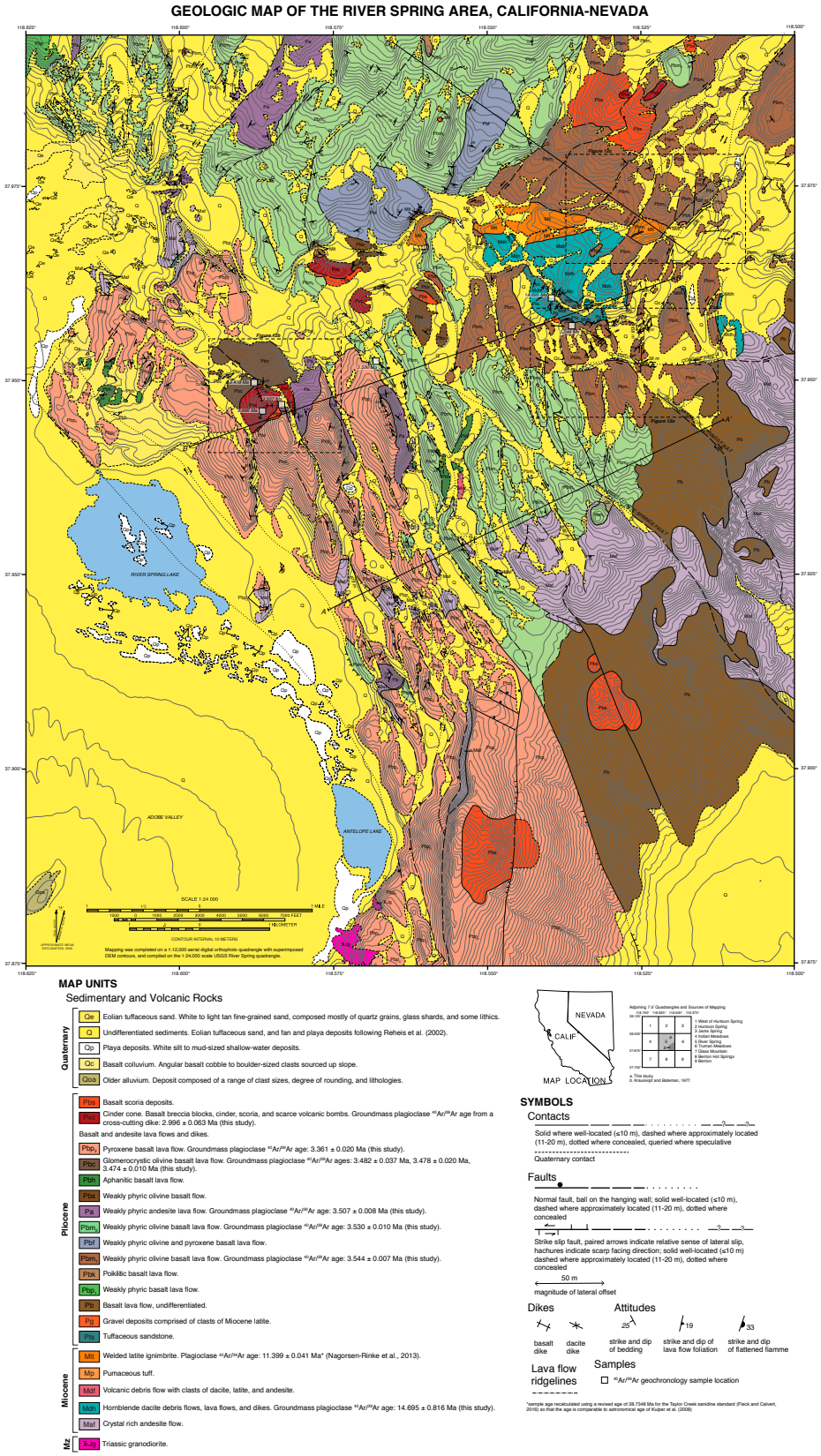

Figure 7. (A) Geologic map of the River Spring area California-Nevada, USA (1:24,000 scale). See Figure 3 for location. Dashed boxes show locations of Figure 12A–12C. Figure 7A is intended to be viewed at a width of 20.1 in. To view at full size, please visit https://doi.org/10.1130/GES01636.f7a or access the full-text article on www.gsapubs.org. (*Continued on following page.*)

Figure 7B is intended to be viewed at a width of 25.1 in. To view at full size, please visit https://doi.org/10.1130/GES01636.f7b or access the full-text article on www.gsapubs.org.

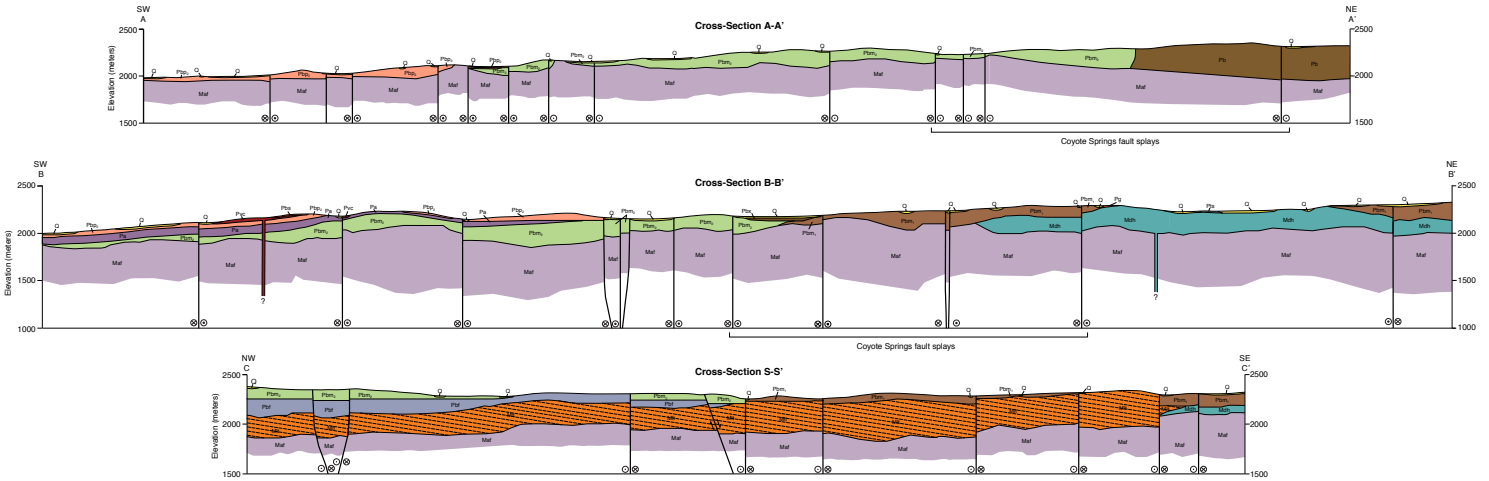

Figure 7 (*continued*). (B) Interpretative geologic cross-sections across the River Spring area. Note that the cross sections are at 1:12,00 scale, half the scale compared to the geologic map shown in A (see A for section locations and unit descriptions). DEM—digital elevation model; USGS—U.S. Geological Survey. Figure 7B is intended to be viewed at a width of 25.1 in. To view at full size, please visit https://doi.org/10.1130/GES01636.f7b or access the full-text article on www.gsapubs.org.

TABLE 1. SUMMARY OF $^{40}Ar/^{39}Ar$ AGES

Sample	Unit	Latitude	Longitude	Material dated	Plateau			Isochron			
					Age (Ma)	±1σ	MSWD	Age (ka)	±1σ	MSWD	^{39}Ar (%) or # of grains
Black Mountain area											
BMF14-007A	Qtc	37.76036	−118.59777	Sanidine	1.976†	0.013	1.17	1.971	0.026	10.01	27 of 30
BMF14-023	Pbp_2	37.73906	−118.57706	GM	3.361	0.020	6.92	3.369	0.029	7.85	80
BMF14-103	Pbc	37.74526	−118.54632	GM	3.474	0.010	1.94	3.475	0.011	2.30	94
BMF14-002A	Pbc	37.72856	−118.57866	GM	3.482*	0.037	20.05	3.464	0.027	21.55	88
BMF14-109	Pbb	37.84060	−118.61644	GM	3.606*	0.060	48.48	3.729	0.039	16.98	92
BMF14-032A	Mrt	37.86852	−118.56925	Sanidine	22.878†	0.051	0.73	22.875	0.051	1.31	33 of 33
River Spring area											
RS13-G181	Pvc	37.94674	−118.58617	GM	2.996*	0.063	2.31	2.940	0.093	2.07	88
RS13-G175	Pbc	37.95001	−118.58662	GM	3.478*	0.020	3.06	3.504	0.021	4.61	68
RS13-G177	Pa	37.94700	−118.58360	GM	3.507	0.008	0.61	3.517	0.013	0.48	68
RS13-G214	Pbm_2	37.95164	−118.56667	GM	3.530	0.010	1.84	3.507	0.019	1.59	73
RS13-G579	Pbm_1	37.95718	−118.53683	GM	3.544	0.007	0.33	3.542	0.014	0.39	84
RS13-G391	Mdh	37.96059	−118.53923	GM	14.695*	0.816	1132.5	14.695	0.204	689.6	100
Huntoon Spring area											
HS001	Pah	38.00258	−118.58675	GM	3.527	0.003	0.55	3.531	0.006	0.34	63
HS335	Pah	38.00396	−118.59138	GM	3.543*	0.011	10.89	3.525	0.033	11.87	81

Notes: Samples were irradiated at the U.S. Geological Survey, Denver, Colorado, USA, TRIGA (training, research, isotopes, General Atomics) reactor using Taylor Creek sanidine at 27.87 Ma as a neutron flux monitor. Listed age results were recalculated to Taylor Creek sanidine at 28.4378 Ma so they are directly comparable to the Kuiper et al. (2008) astronomical framework (Fish Canyon sanidine at 28.198 Ma). Plateau ages are defined by a consecutive series of steps where >50% of ^{39}Ar released is within error. Latitude and longitude recorded in the World Geodetic System 1984.

†Weighted mean age.

*Model recoil age calculated by incorporating age dispersion into the weighted mean age error. GM—groundmass concentrate; MSWD—mean squared weighted deviation.

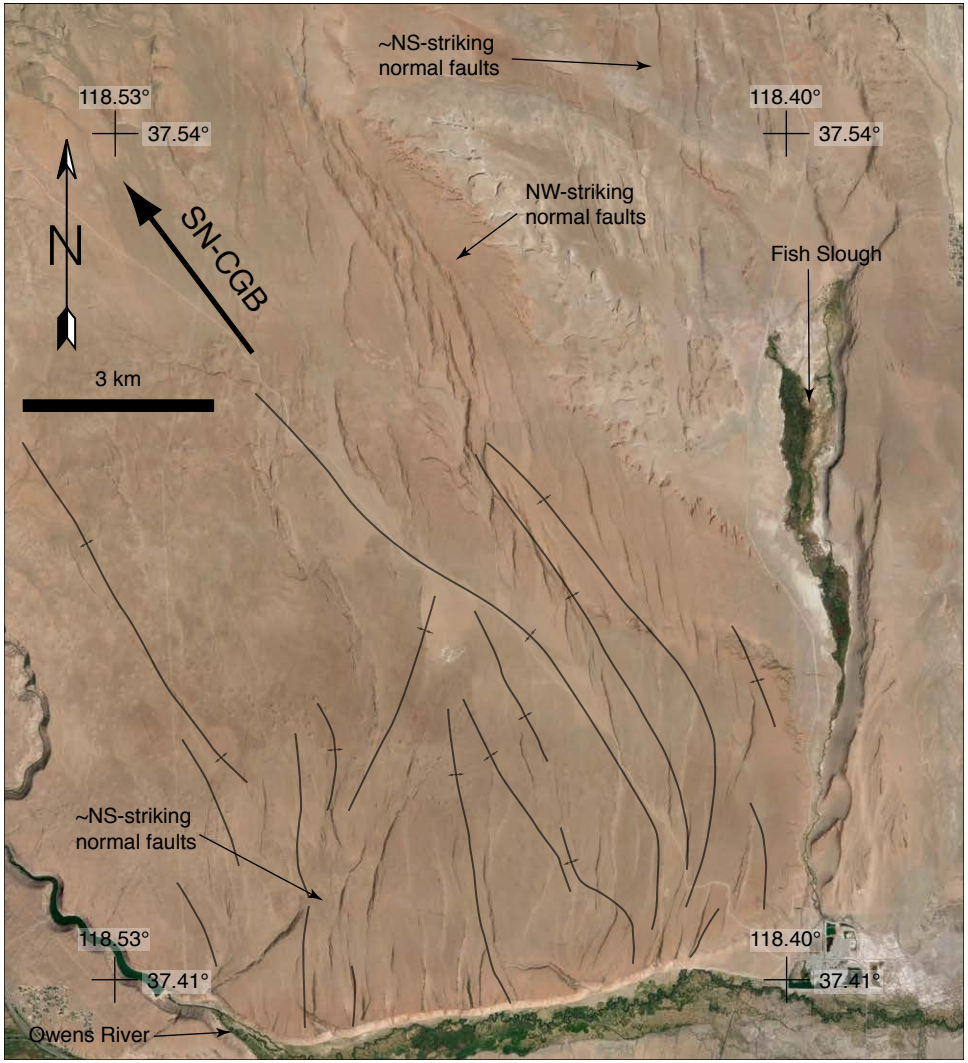

Figure 8. Google Earth image of the southern part of the Volcanic Tableland, California, USA, showing the surface of the Bishop Tuff cut by ~NS-striking normal faults in the southern and northeastern part of the image and NW-striking normal faults in the central part of the image, and traces of folds from Bateman (1965). The NW-striking normal faults are subparallel to the present-day azimuth (323°) of motion of the Sierra Nevada block with respect to the central Great Basin (SN-CGB), which is shown as the heavy arrow (Bennett et al., 2003).

and, combined with magnitude of fault offset measurements, to calculate fault slip rates. Exposed faults within the VBR range from NW- to NE-striking normal faults in the Volcanic Tableland and Black Mountain areas, to NW-striking dextral and ENE- to NE-striking sinistral faults within the River Spring area. These faults cut all units except the youngest Quaternary sedimentary deposits.

Volcanic Tableland

Introduction

The Volcanic Tableland, defined by the surface of the Bishop Tuff, is cut by a set of NS-striking normal faults and NW-striking normal-dextral(?) faults (Bateman, 1965). In the southern part of the Volcanic Tableland, the Bishop Tuff is cut by ~NS-striking normal faults that extend north into the central and eastern part of the tableland. Here, faults curve westward into zones of NW- to NNW-striking, left-stepping, en echelon normal faults (subparallel to SN-CGB motion). In the northern part of the tableland these faults curve eastward to an ~NS-strike (Bateman, 1965; Pinter, 1995) (Fig. 8). Bateman (1965) noted that ~25% of the faults preserved fault striations, most indicating dip-slip normal motion and some indicating oblique-slip; he did not indicate the sense of oblique slip on the latter. The surface of the Volcanic Tableland is also defined by "broad inconspicuous" N- to NW-trending anticlines and synclines (Bateman, 1965) (Fig. 8). Bateman (1965) suggested that NS-dextral shear contributed to the formation of NW-trending anticlinal and synclinal warps and the en echelon normal fault pattern. Pinter (1995) argued that the pattern and geometry of faults indicated faults recorded predominantly normal slip, and that any strike-slip deformation was accommodated by the en echelon pattern of faults or was partitioned into Owens Valley. More recently, Phillips and Majkowski (2011) postulated that arching and flexure of the Bishop Tuff resulted in development of normal faults across the Volcanic Tableland.

Horizontal Extension Rates

To calculate horizontal EW-extension magnitude across the Volcanic Tableland, Pinter (1995) used pace-and-Brunton profile measurements across 38 fault scarps that cut the southern part of the central and western Volcanic Tableland. Assuming 60° ± 10° dips on the normal faults, Pinter (1995) calculated 290 +131/–107 m of horizontal EW-extension. This extension estimate did not include the largest fault scarp in the southern Volcanic Tableland, the ~140 m high, west-dipping, ~NS-striking normal fault scarp in Fish Slough, and a smaller ~13-m-high west-dipping fault scarp east of Fish Slough, both located in the southeastern part of the Volcanic Tableland (Fig. 8). Using the ~140 m and ~13 m heights of these fault scarps and assuming 60° ± 10° fault dip, we calculate ~81 +37/–30 m and ~8 ± 3 m, respectively, of horizontal EW-extension across these two faults. Adding these magnitudes of extension to Pinter's (1995) extension estimate yields a total horizontal EW-extension magnitude of 379 +131/–107 m across the southern Volcanic Tableland. Dividing this magnitude by the U/Pb zircon age measurement for the Bishop Tuff, 766.6 ± 3.1 ka (Chamberlain et al., 2014), yields a minimum horizontal EW-extension rate of 0.5 +0.2/–0.1 mm/yr across the southern Volcanic Tableland (Table 2) somewhat larger than, but within error of, Pinter's (1995) extension rate. Three primary observations indicate the 0.5 +0.2/–0.1 mm/yr extension rate is a minimum estimate: (1) the height of the Fish Slough fault is a minimum because alluvial deposits have accumulated in its hanging wall basin, (2) east of Fish Slough, fault scarps in the Bishop Tuff have been eroded (Bateman, 1965), and (3) faults developed after emplacement of the Bishop Tuff.

Decomposing the ~0.5 mm/yr EW-extension rate into rates parallel and perpendicular to motion of SN-CGB (323°) yields a minimum dextral shear rate of ~0.3 mm/yr and minimum horizontal extension rate of ~0.4 mm/yr parallel and perpendicular, respectively, to the NW-trending en echelon normal fault pattern in the central part of the Volcanic Tableland (Figs. 3 and 8).

Black Mountain Area

Introduction

In the northern part of the Volcanic Tableland, normal faults strike northward through the southern Benton Range into the Black Mountain field area (Rinehart and Ross, 1957; Crowder and Sheridan, 1972; Crowder et al., 1972; Krauskopf and Bateman, 1977; this study) (Fig. 3). In the Black Mountain area, deformation is dominated by normal faulting as evidenced by linear to moderately curved range fronts, exhumation of older units in mountain ranges, and vertically offset Mesozoic granitic basement, Miocene to Pliocene volcanic rocks, and Quaternary tuffs, tilted Miocene to Quaternary volcanic rocks, incised river terraces, and incised alluvial fans (Fig. 6). Normal faults are easily recognized where they cut and offset Miocene to Quaternary units. In granites, however, it is likely that some faults have not been mapped because of the absence of offset markers within the granite as well as difficulty in separating faults from joints when fault striations are not present. Nevertheless, a few faults were easily traced from where they cut the Pliocene–Mesozoic unconformity into Mesozoic plutonic basement (Figs. 6A and 9).

The SN-CGB vector is oblique to the strike of the faults in the Black Mountain area (Fig. 3), suggesting a dextral component of slip on these ~NS-striking normal faults. However, we did not observe fault striations or linear geologic markers that record evidence for a lateral component of slip along these faults. In line with the fault slip partitioning hypothesis proposed for the coexistence of the high-angle, east-dipping normal-slip Sierra Nevada range front fault and the vertical, dextral-slip Owens Valley fault (e.g., Wesnousky and Jones, 1994), we suggest that the faults in the Black Mountain area only record normal dip-slip and the dextral component of slip is spatially partitioned elsewhere (e.g., the White Mountain fault zone). Without fault striations and/or offset linear geologic

TABLE 2. DEFORMATION AND FAULT SLIP RATES ACROSS THE VBR, CALIFORNIA–NEVADA, USA

Volcanic Tableland

Location	Offset marker	Geometry of offset marker	Magnitude of extension (m)	Extension percent	Age of offset marker (ka)	Horizontal (EW) extension rate (mm/yr)
South Volcanic Tableland	Bishop Tuff	~flat lying	379 m +131 m/–107 m	—	766.6 ± 3.1	0.5 +0.2/–0.1

Black Mountain area

Cross-section (domain #)	Offset marker	Dip of offset marker	Approximate extension direction	Extension magnitude (km)	Extension percent	Extension rate (mm/yr)
C-C′ (C)	Base of Pliocene basalt flows	~20°NE	72–252°	1.5 +0.6/–0.4	20%	0.5 ± 0.2
B-B′ (B)	Pliocene–Quaternary/Mzg unconformity	~11°E	85–265°	1.2 ± 0.5	9%	0.4 ± 0.2
A-A′ (A)	Pliocene–Quaternary/Mzg unconformity	~13°NE	60–240°	1.2 ± 0.5	18%	0.4 ± 0.2

River Spring area

Fault zone	Offset marker	Geometry of offset marker	Lateral offset (m)	—	Age of offset marker (Ma)	Lateral slip rate (mm/yr)
D1	Coaldale fault	near vertical	36 ± 5		3.544 ± 0.007	<0.1
D1	Pbm_1 flow edge	steep	108 ± 16		3.544 ± 0.007	<0.1
D1	Pbm_1/Pb	steep	383 ± 115		3.544 ± 0.007	~0.1
D1	Mdh/Mlt contact	steep dip	243 ± 36		11.399 ± 0.041	<0.1
D2	Pbm_1/Pbm_2 contact	steep dip	399 ± 120		3.530 ± 0.010	~0.1
D2	Pbm_1/Pbm_2 contact	steep dip	84 ± 25		3.530 ± 0.010	<0.1
D3–east splay	Pbm_2/Maf contact	steep dip	582 ± 87		3.530 ± 0.010	~0.2
D3–west splay	Pbm_2/Maf contact	steep dip	104 ± 31		3.530 ± 0.010	<0.1
northern D6	Pbc/Pvc contact	steep dip	132 ± 20		2.996 ± 0.063	<0.1
northern D6	Pa/Pvc contact	moderate dip	214 ± 64		2.996 ± 0.063	~0.1
southern D6	Pbp_2/Maf contact	steep dip	679 ± 204		3.361 ± 0.020	0.2 ± 0.1
westernmost strand[§]			281 ± 42		3.348 ± 0.027[§]	~0.1
S1	Pbm_1/Pbk contact	steep dip	66 ± 10		3.544 ± 0.007	<0.1
S1	Pbm_1/Pbk contact (min)	dip unknown	376 ± 188		3.544 ± 0.007	0.1 ± 0.1
S1	Pbm_1/Pbk contact (max)	dip unknown	551 ± 276		3.544 ± 0.007	0.2 ± 0.1
S1	Pbm_1/Mlt contact	steep dip	234 ± 70		3.544 ± 0.007	~0.1
S1	D1 dextral fault	steep dip	57 ± 9		3.544 ± 0.007	<0.1
S6	Pa flow edge	steep edge	156 ± 23		3.507 ± 0.008	<0.1
Coaldale	Dextral fault	near vertical	85 ± 13		3.544 ± 0.007	<0.1

Transects	Offset style	Sum of offset magnitude (m)	Error (m)	Age of offset marker (Ma)	Lateral slip rate (mm/yr)
A-A′	dextral	2029*	255	2.996 ± 0.063	0.7 ± 0.1
B-B′	dextral	805	139	2.996 ± 0.063	0.3 ± 0.1
C-C′	sinistral	766	135	2.996 ± 0.063	0.3 ± 0.1
C-C′	sinistral	941	181	2.996 ± 0.063	0.3 ± 0.1

[§]Dextral offset of unit Pbo (age of 3.348 ± 0.027) by 281 ± 42 m is along the westernmost strand in fault zone D6 in the Adobe Hills area (Nagorsen-Rinke et al., 2013).
*Includes the 281 ± 42 m offset in the Adobe Hills (Nagorsen-Rinke et al., 2013) projected onto the westernmost D6 fault.
Note: VBR—Volcanic Tableland, Black Mountain, and River Spring areas.

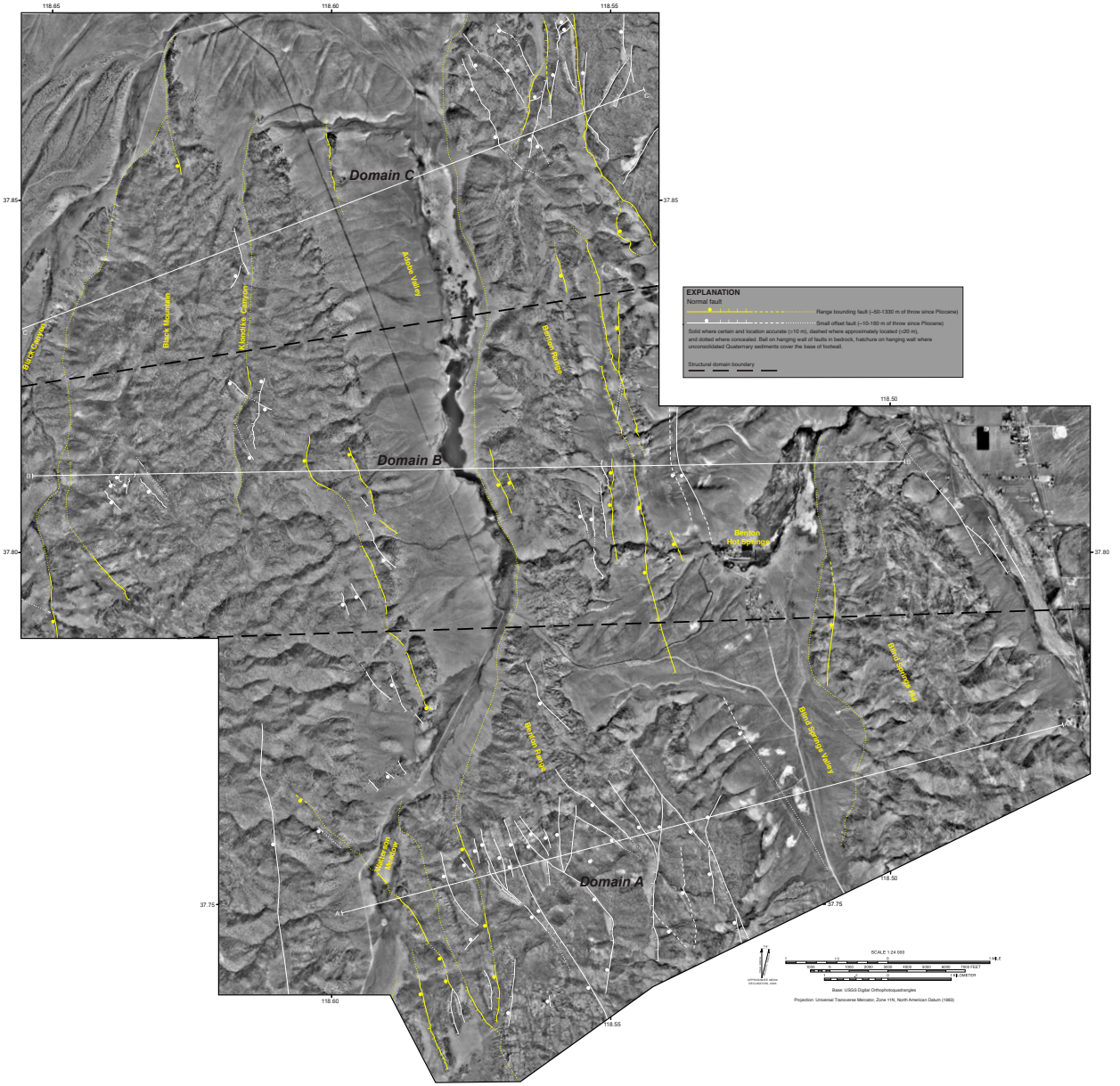

Figure 9. Faults from the geologic map of the Black Mountain area California, USA (see Fig. 6A) compiled on digital orthophotographs highlighting major and minor normal faults and domain boundaries. Range bounding normal faults are shown in yellow and minor normal faults are shown in white. USGS—U.S. Geological Survey. Figure 9 is intended to be viewed at a width of 29.2 in. To view at full size, please visit https://doi.org/10.1130/GES01636.f9 or access the full-text article on www.gsapubs.org.

Figure 9 is intended to be viewed at a width of 29.2 in. To view at full size, please visit https://doi.org/10.1130/GES01636.f9 or access the full-text article on www.gsapubs.org.

markers, we cannot test this hypothesis, thus we cannot conclusively rule out a lesser component of dextral slip along the Black Mountain normal faults.

Fault Geometries, Structural Domains, and Deformation Events

Based on fault strike, length, and amount of throw, we separate normal faults in the Black Mountain area into two faulting styles, although the boundary between styles is gradational (Figs. 6A and 9). Large-offset faults are characterized by ~NS- to NNW-striking, west-dipping range-bounding normal faults that are straight to curvilinear, 1.5–9 km in length, and exhibit ~50–1330 m of dip-slip throw since the Pliocene. Most of these faults are covered by late Quaternary deposits, as a consequence we assume the dip on these faults is the same as on adjacent faults for which we measured a fault dip in the field or calculated a fault dip using a 3-point solution. Small-offset faults are characterized by NW- to NE-striking, steeply (50° to 60°) (Fig. 10A) southwest- to northwest-dipping, straight to curvilinear normal faults ranging from 200 m to 2.5 km in length with ~10–50 m of dip-slip throw (although a few exhibit ~50–160 m of throw) since the Pliocene.

Using fault orientation and average dip of flow foliation and bedding, we define three structural domains within the Black Mountain area (Figs. 6 and 9). Domain A, across the southern third of the map area, is characterized by ~NS- to NNW-striking range bounding large offset normal faults, ~NW- to NE-striking small offset normal faults, and E-NE dipping Pliocene to Quaternary units. Domain B, across the middle third of the map area, is characterized by ~NS-striking range bounding, large offset normal faults, ~NS-striking small offset normal faults, and E-dipping Pliocene to Quaternary units (Figs. 6 and 9). Domain C, located across the northern third of the map area, is characterized by large offset ~NS-striking range bounding normal faults, ~NW- to ~NE-striking small offset normal faults, and E-NE–dipping Miocene to Pliocene units (Figs. 6 and 9).

Deformation episodes in the Black Mountain area can be assessed from the geometric relations between units. Our field observations show that the angular discordance between Miocene and Pliocene units and Pliocene and Quaternary units decreases up section, and older units exhibit a larger magnitude of vertical offset across normal faults compared to younger units indicating at least two deformation events (Fig. 6). Flow foliations measured in Pliocene basalt and andesite flows show these units dip east ~15–30°, at least ~15° less than the underlying Miocene units. We observe no differential offset among Pliocene basalts flows, but do between the Pliocene basalt flows and the overlying Quaternary volcanic tuffs, which dip 5–8° E-NE.

Extension Direction, Magnitude, and Rates

To define the direction of Pliocene–Quaternary extension across each domain within the Black Mountain area, we use tilt direction of Miocene to

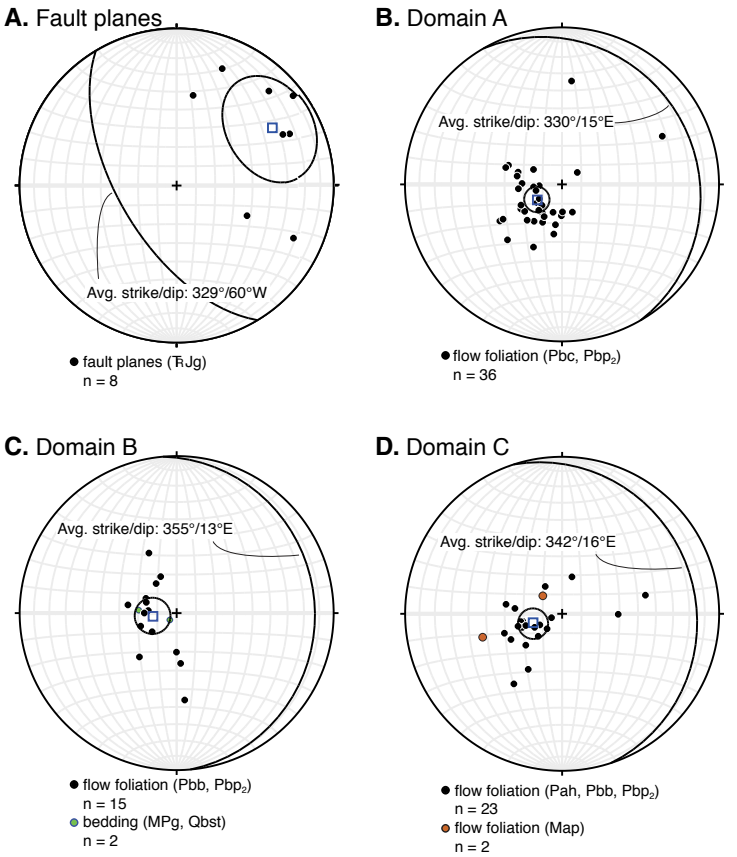

Figure 10. Lower hemisphere, equal area stereonet plots of poles to fault planes in unit TRJg across the Black Mountain area California, USA. (A), and poles to flow foliation and bedding attitudes collected in each structural domain (B, domain 1; C, domain 2; C, domain 3). The mean pole (open blue square) with error (black ellipse), and great circle of average strike and dip are plotted for fault planes in Mesozoic granitic rocks and for flow foliations and bedding measured in Miocene to Pleistocene volcanic rocks and fluvial deposits. Avg.—average.

Quaternary volcanic rocks and fluvial deposits and, to a lesser degree, fault strike and dip. The strike of the faults in the Black Mountain area and their deformation zone width is similar to the normal faults in the southern Volcanic Tableland, thus providing support, albeit non-ideal (see caveat above), for using footwall tilt direction and fault strike and dip to document extension direction across the Black Mountain area.

In domain A, flow foliation attitudes in units Pbc and Pbp_2 yield an average strike and dip of N30W, 15°NE (Fig. 10B). These data, in conjunction with domain A's fault geometry defined by the dominant ~NS- to NNW-striking

normal faults, connected by lesser NW- to NE-striking normal faults, suggest a NE-SW (~60–240°) extension direction (Figs. 6A, 9, and 10B).

In domain B, flow foliation attitudes in units Pbb and Pbp_2 and bedding attitudes in units MPg and Qbst yield an average strike and dip of N5W, 13°NE (Fig. 10C). These data, in conjunction with domain B's fault geometry defined by ~NS-striking range bounding and small offset normal faults, suggest an approximately EW (~85–265°) extension direction (Figs. 6A, 9, and 10C).

In domain C, flow foliation attitudes in units Pah, Pbb, and Pbp_2 yield an average strike and dip of N18W, 16°NE (Fig. 10D). These data, in conjunction with domain C's fault geometry defined by ~NS- to NNW-striking range bounding and ~NW- to NE-striking small offset normal faults, suggest an ENE-WSW (~72–252°) extension direction (Figs. 6A, 9, and 10D).

To calculate the magnitude of extension across the Black Mountain area, we compare the length of palinspastically restored cross-sections (Fig. 6B). We use the nonconformity separating the base of the Pliocene basalt flows and the Quaternary tuffs from the Mesozoic plutonic basement as a marker to palinspastically restore present-day geologic cross-sections. The straight line connecting the two end tie points on each of the three-restored cross-section was used to determine the magnitude of tilt of the marker, which was then rotated counter-clockwise returning the unconformity to its assumed original subhorizontal orientation at the time the Pliocene basalt flows or Quaternary tuffs were emplaced (Fig. 6B).

The restored unconformities on cross-sections A-A′, B-B′, and C-C′, from domains A, B, and C, respectively, yield eastward tilts of ~13°, ~11°, and ~20°, respectively (Fig. 6B). The difference in horizontal distance between end tie points on the present-day geologic cross-sections versus on the palinspastically restored cross-sections yields a magnitude of horizontal extension of 1.2, 1.2, and 1.5 km, indicating 18%, 9%, and 19% extension, respectively (Fig. 6B).

The most significant source of error in our horizontal extension calculations are fault dips, which were determined from field measurements on exposed fault planes, calculated using three point problems on mapped faults, or assigned the same dip as adjacent faults for which dips were known from either of the former methods. To estimate the error associated with the magnitude of extension we palinspastically restored section C-C′, the cross-section that yielded the maximum horizontal extension, using an error in fault dip of ±10°. These restorations yield a range in horizontal extension magnitude from 2.1 km to 1.0 km. Taking into account the range in fault dip, our preferred maximum horizontal extension magnitude across the Black Mountain area is 1.5 +0.6/–0.4 km (an estimated error of ~30%–40%). Using the 40% error as a conservative estimate of uncertainty, we report extension magnitudes of 1.2 ± 0.5 km for cross-sections A-A′ and B-B′ (Table 2).

To obtain a rate of horizontal extension across each structural domain of the Black Mountain area, we divided the magnitude of horizontal extension by the age of the youngest offset Pliocene basalt flow (unit Pbp_2 with an age of 3.361 ± 0.020 Ma). This calculation yields minimum horizontal extension rates of 0.5 +0.2/–0.1 mm/yr, 0.4 ± 0.2 mm/yr, and 0.4 ± 0.2 mm/yr across domains A, B, and C, respectively (Table 2).

River Spring Area

Introduction

NS-striking normal faults at the northern end of the Black Mountain area curve into NW-striking dextral faults that define the southern part of the River Spring area (Krauskopf and Bateman, 1977; this study), and, in turn, NW-striking dextral faults terminate to the northwest into the southeast terminations of NE-striking sinistral faults (Figs. 3, 7A, and 11). In the River Spring area, dextral and sinistral faults are characterized by linear valleys, alternating scarp facing directions along strike, extensional and compressional stepovers, and laterally offset markers including basalt flow margins, near vertical faults, and unit contacts (Fig. 7A). Here, as suggested for the Adobe Hills area (e.g., Reheis et al., 2002; Nagorsen-Rinke et al., 2013), latest Pleistocene and Holocene fault scarps, if developed, have been covered with primary fallout and windblown volcanic ash and small lithics from Mono and Inyo craters to the west. We did not observe exposed fault planes in the field, but the combination of linear fault traces, alternating scarp facing directions, and faults cross-cutting topography indicate that the faults are nearly vertical (dip of 80–90°). NW-striking dextral and NE- to EW-striking sinistral faults cut and offset all Miocene and Pliocene rock units in the River Spring area (Fig. 7).

Fault Geometries, Structural Domains, and Deformation Events

Based on the dominant fault type and fault strike exposed in the River Spring area, we define three fault zone domains: (1) Domain D is located south of Pizona Creek across the southern approximately two-thirds of the field area, and is characterized by NW-striking dextral faults; (2) Domain S is located north of Pizona Creek in the northern approximately one-third of the field area and is characterized by NE-striking sinistral faults; and (3) The E-striking sinistral Coaldale fault defines domain CF which is a narrow zone south of Pizona Creek in the easternmost part of the field area (Figs. 7 and 11).

Domain D is the most areally extensive in the field area and contains the largest number of faults (Figs. 7A and 11). The northern boundary of this domain is located approximately along the trace of Pizona Creek and the western boundary is Adobe Valley; NW-striking dextral faults may be present in Adobe Valley but if so, they are now buried under Quaternary deposits (Fig. 7A). There are six major dextral fault zones (D1–D6) ranging in map trace length from 3.5 to 8.5 km and spaced on average ~1 km (Figs. 7A and 11). The map traces of several faults change from single strands in the southeastern part of the field area into horsetail splays toward the northwest in the central part of the field area.

Domain S is defined by eight major NE-striking sinistral fault zones (S1–S8) that extend from the northern end of the field area southwestward ~3.0–3.6 km toward Pizona Creek (Figs. 7A and 11). These faults are spaced on average ~1.5 km, and similar to the dextral faults, several sinistral faults in domain S at

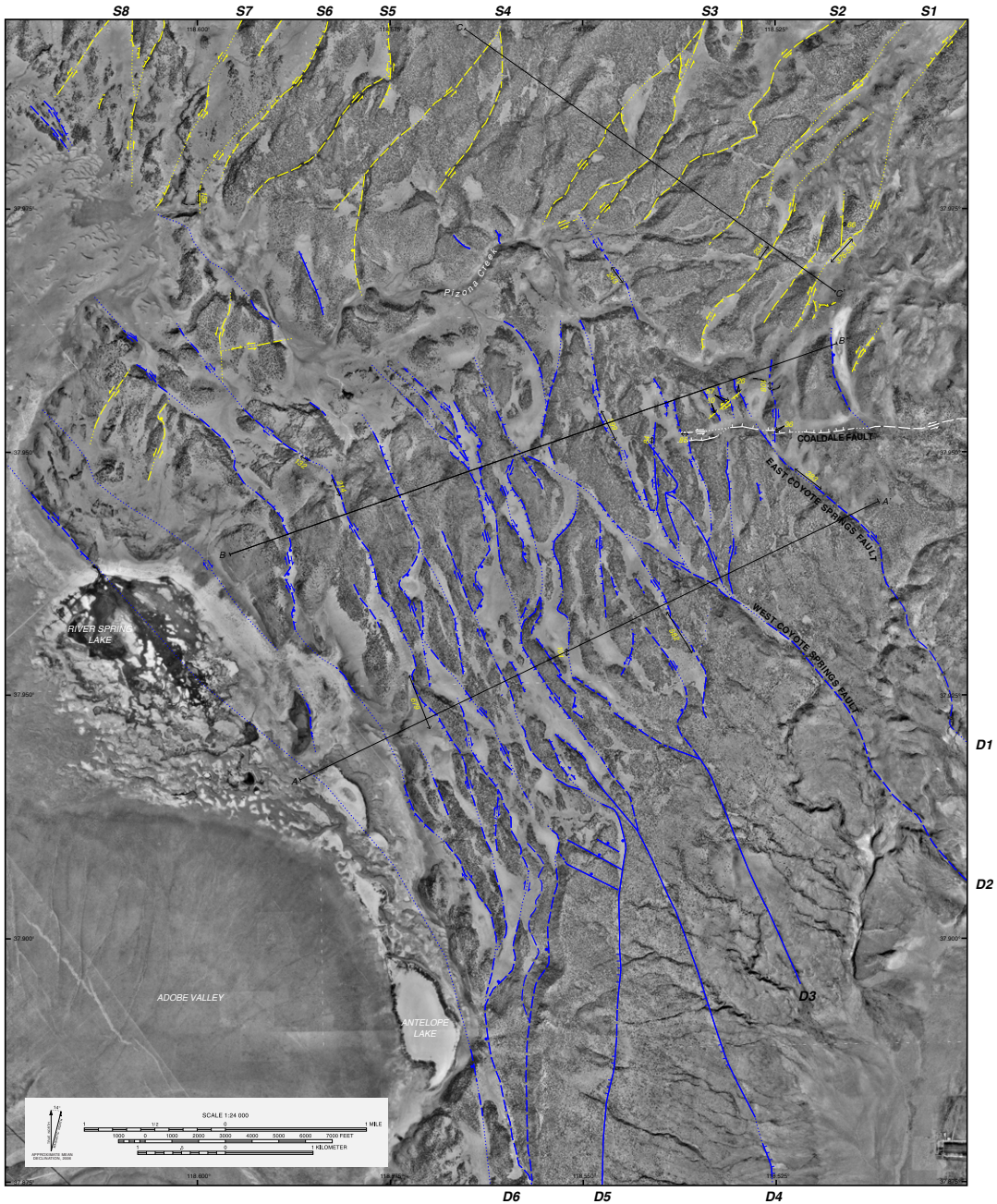

Figure 11. Faults from the geologic map of the River Spring quadrangle California-Nevada, USA (see Fig. 7A) compiled on digital orthophotographs highlighting primary fault zones and locations of measured lateral offset. Dextral faults are shown in blue; sinistral faults are shown in yellow, and the Coaldale fault is shown in white. Fault line style, solid ball, hachures, and paired arrows are defined in Figure 7A. See text for discussion of slip rate calculations along transects A-A′, B-B′, and C-C′. Figure 11 is intended to be viewed at a width of 19.8 in. To view at full size, please visit https://doi.org/10.1130/GES01636.f11 or access the full-text article on www.gsapubs.org.

Figure 11 is intended to be viewed at a width of 19.8 in. To view at full size, please visit https://doi.org/10.1130/GES01636.f11 or access the full-text article on www.gsapubs.org.

the northeastern end of the map area, or just to the north of the map area, splay from a single strand into several strands toward the central part of the field area.

The ~3.4-km-long western end of the EW-striking sinistral Coaldale fault—which extends ~45 km across the southern boundary of the Mina deflection (Bradley, 2005; Lee et al., 2006; Tincher and Stockli, 2009)—defines domain CF in the River Spring area (Figs. 7A and 11). At the intersection of the three domains (Figs. 7A and 11), the EW-striking sinistral Coaldale, NE-striking sinistral, and NW-striking dextral faults record mutually cross-cutting relationships, indicating that slip along both sinistral and dextral faults was contemporaneous.

The River Spring area records development of paleotopography during and after deposition of Miocene units suggesting at least one pre-Pliocene deformation event (Fig. 7). North of Pizona Creek, the outcrop pattern of unit Mlt (ca. 11.4 Ma) defines an ~600-m-wide × ~3.7-km-long EW-trending paleovalley or channel developed within unit Mdh (ca. 14.7 Ma) (Fig. 7A). The southern margin of this paleovalley is defined by a vertical contact between the younger Mlt and the older Mdh; the northern margin is covered by younger Pliocene basalt flows. As observed in the Adobe Hills (Nagorsen-Rinke et al., 2013), tilted flow foliation measurements and paleorelief in Miocene units also suggest an episode of deformation prior to emplacement of the Pliocene basalt and andesite lavas.

Although faults documented to be Miocene in age were not observed in the River Spring field area, previous work in the nearby Adobe Hills and Queen Valley regions suggested that Miocene units underwent uplift and tilting (Tincher and Stockli, 2009; Nagorsen-Rinke et al., 2013) prior to the Pliocene. In addition, map, structural, paleomagnetic, and geochronologic data (e.g., Dilles and Gans, 1995; Stockli et al., 2003; Tincher and Stockli, 2009; Rood et al., 2011; Dubyoski et al., 2016; Mayberry and Lee, 2017; Hoxey et al., 2018) indicate deformation occurred during the Miocene over a broad region encompassing the central Walker Lane, the northwestern part of the Mina deflection, and northern part of the ECSZ.

The second deformation event in the River Spring area is defined by the NW-striking dextral faults, which strike subparallel to SN-CGB motion, NE-striking (average of ~N38E) sinistral faults, and the EW-striking Coaldale sinistral fault that cut and offset Miocene and Pliocene rock units (Figs. 7A and 11).

Magnitude of Dextral Offset and Fault Slip Rates

Dextrally offset geologic markers include lava flow ridge lines, vertical faults, and unit contacts. Measurements were made on a 1:12,000 geologic map or in the field using a handheld GPS unit. Errors associated with lateral offset measurements include GPS survey points (~3 m), visually defining the location of intersection between the offset marker and fault, and the geometry of the marker (strike and dip) relative to the vertical faults. The latter two errors are the larger of the three, and, although difficult to quantify, we assign an error of 15% for a well-defined intersection, such as a vertical depositional contact (e.g., paleovalley wall) cut and offset by a vertical fault, and a more conservative error of at least 30% for less well-defined intersections such as moderately dipping contact cut and offset by a vertical fault. Fault slip rates were calculated from the measured offset and age of youngest offset unit, and the error in fault slip rate is the standard deviation of associated offset and age error. Calculated fault slip rates are a minimum since the late Pliocene because this is the maximum age for onset of fault slip (Table 2).

In domain D, we documented dextral offset of between 36 ± 5 m and 679 ± 204 m on four of the six NW-striking dextral fault zones (Table 2; Figs. 7A and 11). Combining these offset measurements with age of the cut and offset Pliocene volcanic rocks, 2.996 ± 0.063 Ma to 3.544 ± 0.007 Ma, yields a minimum dextral fault slip rate of <0.1–0.2 ± 0.1 mm/yr on each fault (Table 2).

Fault zones D1 and D2, located in the southeastern most region of the River Spring map area, are splays spaced ~1.2 km apart that define the northwestern continuation of the Coyote Springs fault (Lee et al., 2009b) (Figs. 7A and 11). Approximately 700 m south of the Coaldale fault, the east Coyote Springs fault (fault zone D1) offsets a steeply dipping Pbm_1-Pb contact 383 ± 115 m (Figs. 7A, 11, and 12A), which combined with the $^{40}Ar/^{39}Ar$ age of 3.544 ± 0.007 Ma for unit Pbm_1, indicates a minimum dextral slip rate of ~0.1 mm/yr. To the northwest of this offset, fault zone D1 splays to the north and northwest. The north splay cuts and offsets the near vertical sinistral Coaldale fault 36 ± 5 m and to the north of that, this splay cuts and dextrally offsets a steeply dipping Pbm_1 flow edge 108 ± 16 m (Figs. 7A, 11, and 12A). Since unit Pbm_1 is offset at both of these locations along this fault splay, fault offset magnitude combined with the 3.544 ± 0.007 Ma age for this unit yields a minimum dextral slip rate of <0.1 mm/yr (Table 2). The northern termination of the D1, where it extends into domain S north of Pizona Creek, cuts and offsets a steeply dipping contact between the 11.399 ± 0.041 Ma unit Mlt (Nagorsen-Rinke et al., 2013) and underlying older unit Mdh 243 ± 36 m (Figs. 7A and 11). This northern trace of the East Coyote Springs fault, like the southern trace, dextrally offsets unit Pbm_1 indicating slip after emplacement of unit Pbm_1 and a minimum Pliocene dextral slip rates of ~0.1 mm/yr.

Fault zone D2 (Figs. 7A and 11), the west Coyote Springs fault, splays northwestward from a single strand into several strands. A well-defined steeply dipping contact between the 3.530 ± 0.010 Ma unit Pbm_2 and the older Pbm_1 is dextrally offset 399 ± 120 m along the fault splay ~825 m west of the western termination of the Coaldale fault (Figs. 7A) indicating a minimum dextral slip rate of ~0.1 mm/yr (Table 2). About 550 m to the east, a N-striking D2 splay dextrally offsets the same contact 84 ± 25 m (Figs. 7A, 11, and 12A) yielding a minimum dextral slip rate of <0.1 mm/yr.

Fault zone D3 splays northwestward from a single strand into three main NW- to N- striking splays spaced ~300–800 m apart (Figs. 7A and 11). The easternmost D3 fault splay cuts and offsets a moderately dipping contact between the 3.530 ± 0.010 Ma unit Pbm_2 and older unit Maf 582 ± 87 m and a western strand cuts a steeply dipping contact between the same two units 104 ± 31 m (Figs. 7A). Combining these offset measurements with the age of Pbm_2 yields a minimum dextral slip rate of ~0.2 mm/yr along fault zone D3 (Table 2). Offset markers were not observed along the fault zones D4 and D5.

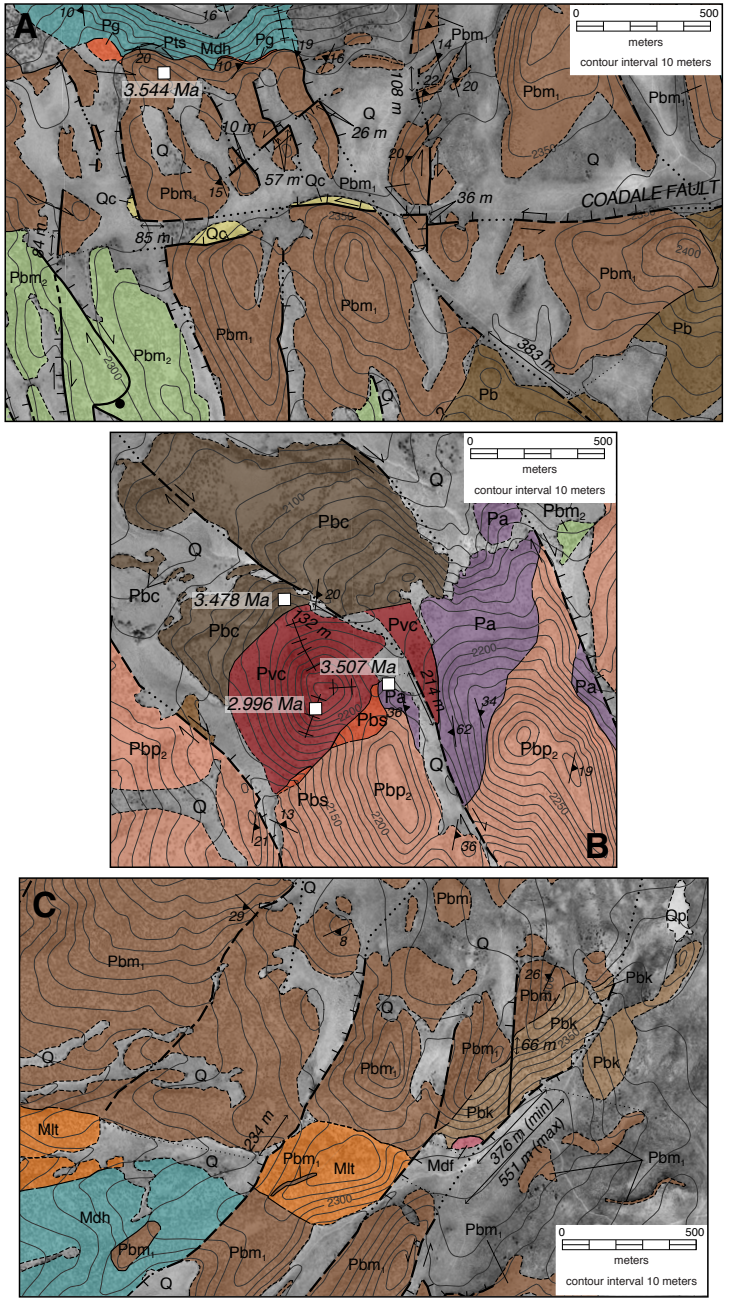

Figure 12. Detailed fault maps superimposed on digital orthophotographs and digital elevation map-generated contours showing dextral and sinistral offset of geologic features in the River Spring area California-Nevada, USA (see Figs. 7A and 11). (A) Offset markers along dextral fault zones D1 and a D2 fault splay, southwestern most fault strand in zone S1, and the Coaldale fault. (B) Two dextrally offset markers along the middle splay of fault zone D6. (C) Sinistral offset along fault zone S1. Locations of figures are shown in Figure 7A. See text for detailed discussion of offset measurements.

Fault zone D6, the westernmost fault zone, is characterized by three fault strands that splay north to westward into several NW-striking dextral faults (Figs. 7A and 11). These splays typically have longer traces than the other fault zones and are typically spaced ~250–725 m apart. Along the middle splay, three dextrally offset markers are exposed (Figs. 7A, 11, and 12B). The central part of this fault cuts and dextrally offsets a steeply dipping unconformity between unit Pbp_2 and older unit Maf 679 ± 204 m, indicating a minimum late Pliocene dextral slip rate of 0.2 ± 0.1 mm/yr. Farther north, in the vicinity of a cinder cone, the steeply dipping contact between the 2.996 ± 0.063 Ma Pvc and the older Pbc is dextrally offset 132 ± 20 m and the Pvc-Pa contact, oblique to the strike of the fault, is dextrally offset 214 ± 64 m, yielding a minimum slip rate of <0.1 to ~0.1 mm/yr (Figs. 7A, 11, and 12B; Table 2). The westernmost exposures of dextral faults in fault zone D6 define the eastern boundary of the Adobe Valley; River Spring is likely developed along the western most D6 fault (Figs. 7A and 11). These faults project northwest along strike into NW-striking dextral faults in the Adobe Hills mapping area where Nagorsen-Rinke et al. (2013) documented dextral offset of 281 ± 42 m, yielding a ~0.1 mm/yr dextral fault slip rate. Assuming this offset magnitude, and timing, are the same along the length of these faults indicates a minimum Pliocene dextral slip rate of ~0.1 mm/yr along the westernmost D6 fault strand.

To calculate a total minimum dextral offset magnitude and slip rate across domain D in the River Spring area, we summed offsets along two transects, A-A′ and B-B′, that are orthogonal to the strike of the dextral faults and cross all faults with measurable dextral offsets (Figs. 7A and 11). Transects A-A′ and B-B′ yield minimum dextral offset magnitudes of 2029 ± 255 m and 805 ± 139 m, respectively (Table 2). Combining these minimum net dextral offsets with the age of the youngest offset Pliocene volcanic rock, unit Pvc, with an age of 2.996 ± 0.063 Ma, yields an estimated net minimum dextral fault slip rate of 0.7 ± 0.1–0.3 ± 0.1 mm/yr, respectively (Table 2). These are minimum dextral fault slip rates because of the lack of measurable offset geologic markers on two of the major dextral fault zones, D4 and D5, and because faulting began after emplacement of the Pliocene basalt field (see below).

Although we did not observe offset markers across fault zones D4 and D5, by comparing their geomorphic expression to the fault zones with measured dextral offsets we estimate a dextral fault slip rate for these fault zones. The southern part of fault zone D4 is dominated by one geomorphically well expressed fault, whereas the northern part, in proximity to Pizona Creek, is characterized by several closely spaced (~130 m apart) splays. The geomorphic

expression of the southern part of fault zone D4 is as good, if not better than fault zone D3 suggesting that fault zone D4 records an estimated fault slip rate of ≤0.1 mm/yr. The southern part of the fault zone D5 has a similar geomorphic expression as fault zone D4, suggesting a dextral slip rate of ~0.1 mm/yr along this fault zone. If our assumptions in correlating slip rate to geomorphic features are valid, then our preferred net minimum dextral fault slip rate across the entire River Spring area is ~0.8–0.9 mm/yr.

Magnitude of Sinistral Offset and Fault Slip Rates

Domain S, the NE-striking sinistral fault zone, exposes few offset markers (faults, unit contacts, and flow edges) (Figs. 7A, 11, and 12C). Two of eight NE-striking sinistral fault zones expose geologic makers that are offset between 57 ± 9 m and 551 ± 276 m (Figs. 7A, 11, and 12C; Table 2). Combining these lateral offset measurements with the age of the cut and offset Pliocene volcanic rocks, 3.544 ± 0.007 Ma and 3.507 ± 0.008 Ma, yields a minimum sinistral fault slip rate of ≤0.1–0.2 ± 0.1 mm/yr/fault (Table 2).

Fault zone S1, located in the northeastern region of the River Spring area (Figs. 7A, 11, and 12C), is composed of several fault splays that, based on interpretation of aerial photographs, merge northeastward into a single fault off the map area. One short eastern splay sinistrally offsets a steep contact between unit Pbm_1 and older unit Pbk 66 ± 10 m; given the age of 3.544 ± 0.007 Ma for unit Pbm_1, this fault records a slip rate of <0.1 mm/yr. Another of the eastern most fault splays cuts and offsets a moderate dipping stratigraphic contact between unit Pbm_1 and underlying unit Pbk. The contacts between units Pbm_1 and Pbk on both sides of the fault are buried by Quaternary deposits, thus we measured a minimum and maximum sinistral offset of 376 ± 188 m and 551 ± 276 m, respectively (Figs. 7A, 11, and 12C). Combining the range in offset magnitude and age of unit Pbm_1 yields a sinistral slip rate range of ~0.1 mm/yr to 0.2 ± 0.1 mm/yr. Across one of the central fault splays, a steeply dipping unconformity between a Pbm_1 basalt flow and underlying unit Mlt is sinistrally offset 234 ± 70 m; combined with the age of unit Pbm_1 yields a sinistral slip rate of ≤0.1 mm/yr. A southwesternmost fault strand in zone S1, located ~650 m northeast of the western termination of the Coaldale fault, cuts and sinistrally offsets three dextral fault strands 26 ± 4 m, 57 ± 9 m, and 10 ± 2 m within unit Pbm_1 (Fig. 7A, 11, and 12A), indicating a sinistral slip rate of <0.1 mm/yr (Table 2).

Fault zone S6, located in the northwestern region of the River Spring area, is composed of a single fault strand that appears to splay southwestward into two splays (Figs. 7A and 11). The westernmost fault splay offsets a Pa flow edge 156 ± 23 m. Combining the fault offset measurement magnitude with the age of 3.507 ± 0.008 Ma for unit Pa yields a minimum sinistral fault slip rate of <0.1 mm/yr along the fault splay (Table 2). Offset geologic markers were not observed on the remaining sinistral fault zones (S2, S3, S4, S5, S7, and S8).

Projecting the sinistral offset along fault zones S1 and S6 to transect C-C′ and assuming constant offset magnitude along strike, yields a net minimum sinistral offset of 766 ± 135 m to 941 ± 181 m across domain S (Figs. 7A and 11; Table 2). Combining this net sinistral offset with the age of the offset Pliocene volcanic rocks (3.544 ± 0.007 Ma to 2.996 ± 0.063 Ma) yields an estimated net sinistral fault slip rate of 0.3 ± 0.1 mm/yr (Table 2). Due to the lack of measurable offset geologic markers on the remaining major sinistral fault zones (S2, S3, S4, S5, S7, and S8) and because faulting began after emplacement of the basalt flows, our calculated net sinistral offset along transect C-C′ is a minimum estimate.

As we did with dextral faults, we compare the geomorphic expression of the fault zones with measured offsets and calculated slip rates to the fault zones without documented offsets to calculate a preferred minimum sinistral fault slip rate across the River Spring area. The morphologic expression of fault zones S2, S3, S4, and S5 appears to be nearly as well developed as fault zone S1; the similarity in geomorphic expression suggests that these four fault zones record an estimated fault slip rate of ~0.1 mm/yr/fault. Fault zones S7 and S8 are each defined by one or more fault strands and their morphological expression appears less than fault zone S6, suggesting an estimated fault slip rate of <0.1 mm/yr/fault zone. If our geomorphic-slip rate correlations are valid, then our preferred net minimum sinistral fault slip rate across the River Spring area is ~0.7–0.9 mm/yr.

The western termination of the ~EW-striking sinistral Coaldale fault, which can be traced for 45 km to the east of River Spring, is exposed in the field area and cuts unit Pbm_1 and Pbm_2 (Figs. 7A and 11). The westernmost exposure of the Coaldale fault diverges into two splays that are spaced ~80 m apart; these splays and NNW-striking dextral faults in fault zones D1 are mutually cross-cutting (Figs. 7A, 11, and 12A). The southern splay of the Coaldale fault cuts and offsets a near vertical dextral fault trace 85 ± 13 m indicating a slip rate of <0.1 mm/yr.

In summary, the calculated minimum net fault slip rate across the NW-striking dextral fault domain is 0.7 ± 0.1 mm/yr; our preferred minimum fault slip rate is 0.8–0.9 mm/yr. Calculated Pliocene minimum net fault slip rate across the NE-striking sinistral faults is 0.3 ± 0.1 mm/yr; our preferred minimum fault slip rate is ~0.7–0.9 mm/yr. The western termination of the Coaldale fault records <0.1 mm/yr of sinistral slip.

Summary of Volcanic and Deformation Histories in the VBR

The VBR, located across the transition from the northwestern ECSZ into the southwestern part of the Mina deflection (Fig. 3), records a history of Miocene to Quaternary volcanism, and Miocene and late Pliocene to present-day fault slip. Miocene volcanism and deformation is preserved in the Black Mountain and the River Spring areas. Although the exact style and magnitude of this volcanic and deformation event is not well-defined, it is likely similar to the better documented pulse of Miocene volcanism, extension, and dextral slip in the central WLB, Mina deflection, and northern ECSZ suggesting this event is regional (e.g., Oldow et al., 1994; Dilles and Gans, 1995; Surpless et al., 2002;

Stockli et al., 2002, 2003; Tincher and Stockli, 2009; Rood et al., 2011; Dubyoski et al., 2016; Mayberry and Lee, 2017; Hoxey et al., 2018).

A Pliocene basalt volcanic and faulting event is preserved in the Black Mountain and River Spring areas where faults cut Pliocene and older plutonic, volcanic, and sedimentary rocks. In the Black Mountain area, the absence of angular unconformities between the Pliocene basalt lavas, but between the lavas and the younger early Quaternary Tuff of Taylor Canyon, indicates that the Pliocene episode of deformation began after an ~550,000-year-long period of basalt volcanism (ca. 3.544–2.996 Ma) but before eruption of the ca. 1.976 Ma Tuff of Taylor Canyon. Basalt volcanism of this age and a Pliocene pulse of normal, dextral, and sinistral faulting occurred throughout this part of the ECSZ-Mina deflection region (Fig. 3), including the Adobe Hills and Huntoon Spring areas (Nagorsen-Rinke et al., 2013; Hogan, 2014), the Queen Valley region (Stockli et al., 2003; Tincher and Stockli, 2009), the Saline Range (Sternlof, 1988), eastern Inyo Mountains (Lee et al., 2009a), and the southern Inyo Mountains (Larsen, 1979; Casteel, 2005).

Volcanism and faulting continues through the Quaternary to the present day as evidenced by eruption of several Quaternary volcanic units in the VBR (e.g., Bateman, 1965; Krauskopf and Bateman, 1977; Metz and Mahood, 1985; Pinter, 1995; Chamberlain et al., 2014; this study), faults that cut and tilt Quaternary and older units (e.g., Rinehart and Ross, 1957; Bateman, 1965; Crowder et al., 1972; Crowder and Sheridan, 1972; Krauskopf and Bateman, 1977; Lee et al., 2009b; this study) and recent earthquakes (Lienkaemper et al., 1987; http://www.ncedc.org/recenteqs/) (Fig. 2).

DISCUSSION

Kinematics of Fault Slip Transfer: Northern Eastern California Shear Zone to Mina Deflection

Our field-based investigations show that the geometry, style, and kinematics of fault slip varies from south to north across the VBR. Approximately NS-striking normal faults exposed across the southern Volcanic Tableland curve westward into NW-striking en echelon, normal-dextral(?) faults in the central part of the Volcanic Tableland, which curve eastward into ~NS-striking normal faults in the Black Mountain region. The normal faults in the Black Mountain region extend northward curving westward into NW-striking dextral-normal(?) faults in the southern River Spring area, and these faults abut NE-striking sinistral faults, characteristic of the Mina deflection, in the northern River Spring and Adobe Hills regions. These fault styles and orientations are consistent with the Nagorsen-Rinke et al. (2013) kinematic fault slip model (Fig. 4). Below, we evaluate the model's predicted fault slip rates using our new minimum and preferred fault slip rates across the VBR, combined with published estimates for fault slip rates across the northern ECSZ-southwestern Mina deflection transition (Lifton, 2013; Nagorsen-Rinke et al., 2013; Kirby et al., 2006, 2008; Lee et al., 2006, 2009b; Tincher and Stockli, 2009; Bradley, 2005; this study) (Fig. 13).

In the Nagorsen-Rinke et al. (2013) kinematic model, dextral slip along the Owens Valley fault is partitioned northwestward onto the Volcanic Tableland and northeastward onto the White Mountain fault zone (Figs. 3 and 13A). To expand upon the Nagorsen-Rinke et al. (2013) kinematic model (Fig. 13A), we compare two different models (models 1 and 2) for northward partitioning of dextral slip along the Owens Valley fault (cf. Figs. 13B and 13C). Our kinematic models, which simplify the more complicated natural fault geometries, kinematics, and rates, were developed under the following assumptions. (1) Fault geometries and orientations have been simplified (cf. Figs. 3 and 13). (2) All fault slip rates have remained constant through time. (3) We treat all published and new minimum fault slip rates in the models as absolute rates and do not take into account the errors in the slip rate estimates. (4) Our models are rotationally static in that vertical axis rotations are not taken into account. (5) Although the Nagorsen-Rinke et al. (2013) model did not explicitly predict an ~EW-horizontal extension rate across the Volcanic Tableland, the near parallelism of normal faults in the southern Volcanic Tableland and the Black Mountain region, similar deformation zone widths, and their linkage via NW-striking normal-dextral(?) faults, indicates that the predicted deformation across the Black Mountain range is the same as for the southern Volcanic Tableland. We therefore add a predicted WSW-ENE–trending horizontal extension rate of ~0.6 mm/yr across the southern Volcanic Tableland to the Nagorsen-Rinke et al. (2013) model (Fig. 13A). (6) We assign a dextral slip rate of 2.8 mm/yr on the northern Owens Valley fault, the minimum rate Kirby et al. (2008) estimated. (7) In model 1, we partition 2.8 mm/yr of dextral slip on the Owens Valley fault northward into two orthogonal components, 0.4 mm/yr of WSW-ENE extension across the Volcanic Tableland with the remaining slip (2.7 mm/yr) partitioned solely onto the NNW-striking White Mountain fault zone (Fig. 13B). (8) In model 2, we present an alternative scenario for partitioning Owens Valley fault slip. In this model, we partition Owens Valley fault slip into 1.9 mm/yr of dextral shear onto the NNW-striking dextral White Mountain fault zone, the minimum rate estimated by Lifton (2013). The residual Owens Valley fault slip is partitioned into two additional components, 0.5 mm/yr of EW-extension across the southern Volcanic Tableland and 0.8 mm/yr of NNW-dextral slip onto the Round Valley fault, a segment along the Sierra Nevada frontal fault zone, via a northwest contractional stepover across the Coyote Warp (Fig. 13C).

Model 1

In model 1, 2.8 mm/yr of dextral slip along the Owens Valley fault is partitioned northward into two components, 0.4 mm/yr of WSW-ENE extension across the southern Volcanic Tableland and 2.7 mm/yr of NNW-dextral shear along the White Mountain fault zone. Our new EW-extension rate of ~0.5 mm/yr across the southern Volcanic Tableland is the same, within error, as the predicted model rate, but its trend is ~12° clockwise from the predicted extension direction. We decompose our estimated EW-extension rate of ~0.5 mm/yr into two orthogonal components, ~0.3 mm/yr of dextral shear parallel to the

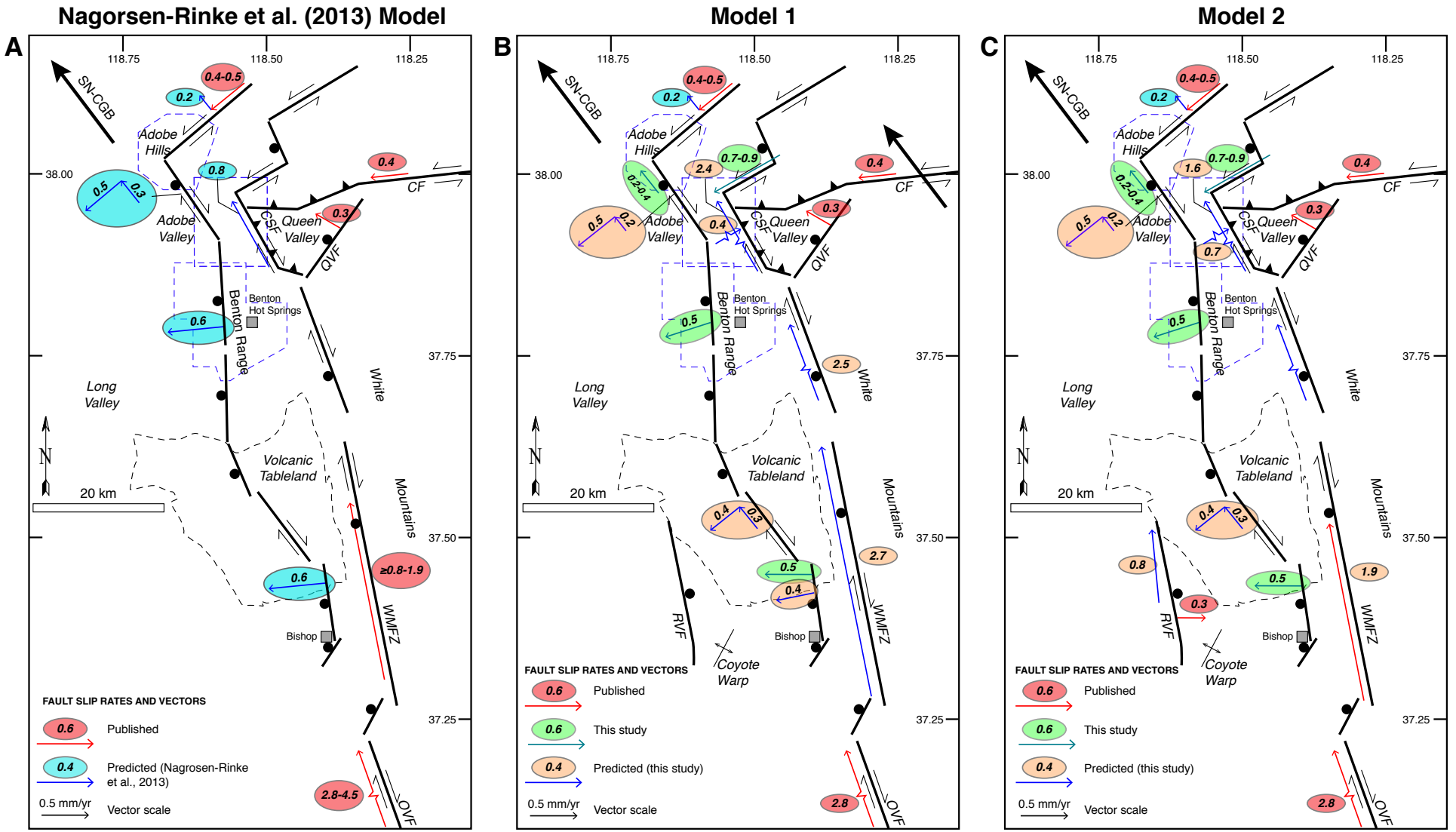

Figure 13. Kinematic fault slip models across the transition from the northwestern eastern California shear zone to the southwestern Mina deflection, California–Nevada, USA (cf. Fig. 3). (A) The Nagorsen-Rinke et al. (2013) kinematic model. (B) Kinematic Model 1. (C) Kinematic Model 2. Dashed black line bounds the Volcanic Tableland; blue dashed polygons show the locations of map areas Black Mountain (south), River Spring (middle), and Adobe Hills (Nagorsen-Rinke et al., 2013) (north); heavy arrow in the northwest corner of the maps shows the present-day azimuth of motion of the Sierra Nevada block with respect to the central Great Basin (SN-CGB) (Bennett et al., 2003). Fault symbols defined in Figure 2; fault abbreviations are defined in Figures 2B and 3. Figures modified from Nagorsen-Rinke et al. (2013) and Lee et al. (2009b). See text for discussion.

NW-striking faults—which strike parallel to motion of SN-CGB—in the central Volcanic Tableland and ~0.4 mm/yr of NE-SW horizontal extension perpendicular to the dextral shear (Figs. 13B). Deformation across the Volcanic Tableland is kinematically transferred, via NNW- to NS-striking normal faults, northward into the Black Mountain field area, where Nagorsen-Rinke et al. (2013) predicted 0.6 mm/yr of ENE-WSW extension. Our observed Pliocene extension rate of 0.5 ± 0.2 mm/yr across the Black Mountain region is the same, within error, as the predicted rate, but its trend is ~10° anticlockwise from the predicted extension direction (Figs. 13A and 13B).

The model predicted NW-dextral shear rate of 0.3 mm/yr across the southwestern River Spring area (defined by fault zones D5 and D6), which geometrically and kinematically link to normal faults at the north end of the Black Mountain area (cf. Figs. 6A, 7A, 9, 11, and 13), is the same as our preferred minimum dextral shear rate of ~0.2–0.4 mm/yr across these faults (Figs. 13A and 13B). Decomposing ~0.5 mm/yr of NE-SW extension across the Black Mountain area into this part of the River Spring field area yields predicted fault slip values of ~0.2 mm/yr of dextral shear parallel to fault zones D5 and D6, the same to half of our preferred rate, and ~0.5 mm/yr of extension orthogonal to the NW-striking dextral faults. Our observed dextral shear rate along fault zones D5 and D6 may be larger (i.e., 0.4 mm/yr) than model 1's predicted model rate of 0.2 mm/yr because either: (a) our assumption that minimum slip rates equal absolute rates across the Volcanic Tableland and Black Mountain regions is incorrect, (b) ~0.1–0.2 mm/yr of dextral slip along the White Mountain fault zone is transferred across the northern end of the Volcanic Tableland onto these dextral faults (cf. Smith and Priestly, 2000) (Figs. 3 and 13B), and/or (c) our assumption of irrotational deformation across the southwestern Mina deflection is not valid (cf. Dickinson, 1996). The NE-SW extension rate across the southwestern River Spring area is the same as that predicted by the Nagorsen-Rinke et al. (2013) model (Figs. 13A and 13B), yet normal offset along these dextral faults has not been observed (Nagorsen-Rinke et al., 2013; this study). In line with Nagorsen-Rinke et al. (2013), we speculate that the NE-SW extension occurred on a normal fault (or faults) now buried under valley fill along the northeastern margin of Adobe Valley. Extension across this normal fault system would explain the origin of the valley, which based on gravity profiles, is estimated as ~1830 m deep (Higgins et al., 1985). The inferred westernmost fault strand in zone D6 may be one of these faults (Figs. 7A and 13B). The minimum dextral shear rate along fault zones D5 and D6 predicts ~0.2 mm/yr of NW-SE extension across sinistral faults in the Adobe Hills region, the same predicted rate as in the Nagorsen-Rinke et al. (2013) model, and projection of the NE-SW extension rate of ~0.5 mm/yr across the eastern Adobe Valley onto NE-striking sinistral faults in the Adobe Hills yields ~0.5 mm/yr of sinistral slip consistent with the measured NE-sinistral slip rate of 0.4–0.5 mm/yr in the Adobe Hills region (Nagorsen-Rinke et al., 2013).

Based on our assumption (7) above, model 1's predicted dextral slip rate of 2.7 mm/yr on the White Mountain fault zone is >3 times larger than the minimum Pleistocene estimate of ~0.8 mm/yr (Kirby et al., 2006) to somewhat larger than the minimum late Pleistocene rate of 1.9 +0.5/–0.4 mm/yr (Lifton, 2013), taking into account the error in the Lifton (2013) estimate. If our speculation that ~0.1–0.2 mm/yr of White Mountain fault zone slip is transferred northwestward into the southwestern River Spring area is correct, then model 1 predicts a dextral slip rate of ~2.5 mm/yr along the northern extent of the White Mountain fault zone where it intersects the southern end of Queen Valley (Fig. 13B). Here, dextral slip along the White Mountain fault zone is partitioned into two components: (1) a NE-step onto the Queen Valley normal fault, which accommodates ~0.3 mm/yr of horizontal extension parallel to ~300° (Stockli et al., 2000; Lee et al., 2009b) and (2) a NW-step onto the Coyote Springs fault, with a predicted rate of ~2.5 mm/yr of dextral-oblique slip (Fig. 13B). The 2.5 mm/yr vector trends ~14° clockwise with respect to the average strike of the Coyote Springs fault; decomposing this vector into two orthogonal components yields 2.4 mm/yr of dextral shear parallel to the Coyote Springs fault and 0.4 mm/yr of contraction orthogonal to the fault. Both of these deformation rates along the Coyote Springs fault are significantly larger than the predicted dextral and contractional deformation rates in Lee et al.'s (2009b) model because the slip we use along the White Mountain fault zone is much larger than the value used in their model. A dextral shear rate of ~2.4 mm/yr along the Coyote Springs fault is also considerably larger than the minimum dextral shear rate of ~0.4–0.5 mm/yr we documented across fault zones D1–D4 in the River Spring region, which includes the northwestern splays of the Coyote Springs fault (Figs. 7A, 11, and 13B; Table 2). In this model, the difference in slip rates between our observations and the model may be best explained by the invalidity of our assumptions (2) that minimum fault slip rates are absolute rates, and (4) that the model does not include clockwise rotation along sinistral faults.

Model 2

In model 2 (Fig. 13C), which provides an alternative slip distribution to model 1 (Fig. 13B), 2.8 mm/yr of fault slip along the Owens Valley fault is partitioned northward into 1.9 mm/yr along the White Mountain fault zone (Lifton, 2013) (assumption (8) above) and 0.5 mm/yr of EW-extension across the Volcanic Tableland. If true, this interpretation has two implications. First, to maintain strain compatibility, this partitioning geometry implies that the 2.8 mm/yr of Owens Valley fault slip is partitioned into a third component, ~0.8 mm/yr of NW-dextral slip, which we suggest may be accommodated by a northwest step across the Coyote Warp into the Round Valley fault (Figs. 3 and 13C). In this hypothesis, the anticlinal morphology of the Coyote Warp is the result of a left-stepping restraining bend along a dextral fault system. Our interpretation of the structural setting of the Coyote Warp differs from earlier interpretations. Taylor (1934) suggested that the Coyote Warp defined a scarp ramp located between the southern termination of Sierra Nevada range front faults along Round Valley and the northern termination of the Sierra Nevada range front faults along Round Mountain (Fig. 3). Bateman (1965) proposed that the Coyote Warp was the consequence of broad warping of the Sierra Nevada range front, and Pinter (1995) hypothesized that differential rotations of the

Sierra Nevada and Owens Valley formed the Coyote Warp. If our hypothesis is correct, then the 0.8 mm/yr component of dextral shear may be distributed broadly across the Sierra Nevada range front faults, which strike clockwise with respect to Sierra Nevada–North America motion, thus defining a set of releasing steps in a dextral shear zone (Unruh et al., 2003) and/or if the northern Round Valley fault records right lateral slip, as suggested by Phillips and Majkowski (2011), then this fault may also accommodate some of the partitioned 0.8 mm/yr of dextral shear. Although Phillips and Majkowski (2011) interpreted the dextral offset as the result of tectonics, Unruh et al. (2003) suggested that dextral shear at the northern end of Round Valley region is the consequence of combination of local stresses and deformation associated with movement of magma beneath Long Valley, not regional tectonics.

The second implication of model 2's smaller fault slip rate on the White Mountain fault zone is a smaller predicted dextral slip rate of ~1.6 mm/yr and orthogonal contraction rate of 0.7 mm/yr along the Coyote Springs fault, which reduces, but does not eliminate the discrepancy between observed and model rates in model 1. Like with model 1, the difference in slip rates between our observations and model 2 across the ECSZ-Mina deflection transition is explained by the invalidity of our assumption that minimum fault slip rates are absolute rates, and the absence of clockwise rotation along sinistral faults.

In models 1 and 2, we assume that the minimum estimated slip along the Owens Valley fault, 2.8 mm/yr (Kirby et al., 2008), is the absolute slip rate. Alternatively, if we make the assumption that the geologic dextral slip rate is ~4.1 mm/yr along the northern Owens Valley fault, a rate closer to Kirby et al.'s (2008) maximum estimated rate of 4.5 mm/yr, then partitioning of 4.1 mm/yr into two components, the Volcanic Tableland and the White Mountain fault zone, yields our maximum calculated extension rate of 0.7 mm/yr on the former and a NW-dextral shear rate of 4.0 mm/yr on the latter. Propagation of both of these higher slip rates northward into the southwestern Mina deflection compounds the discrepancies between observed and predicted slip rates.

Kinematics of a Rotational Stepover in a Dextral Fault System

As noted by Nagorsen-Rinke et al. (2013), the three kinematic models proposed for transfer of slip across the Mina deflection were developed for a particular time period (Oldow, 1992, Oldow et al., 1994; Oldow, 2003; Wesnousky, 2005) (Fig. 1), thus implying that the slip transfer mechanism changed from the middle Miocene to present day. Our new geologic mapping did not document normal slip along the NE-striking sinistral faults exposed in the River Spring area, an observation consistent with Nagorsen-Rinke et al.'s (2013) geologic mapping of NE-striking sinistral faults in the Adobe Hills where normal slip was also not documented. Thus, we suggest that the displacement-transfer model (Fig. 1B) (Oldow, 1992; Oldow et al., 1994) and the transtensional model (Fig. 1C) (Oldow, 2003) are not applicable to this part of the Mina deflection since the Pliocene. In line with Nagorsen-Rinke et al.'s (2013) interpretation, we therefore suggest that dextral slip along the NW-striking dextral faults in the River Spring area is transferred northward into clockwise rotation of fault blocks that are bounded by the sinistral faults (e.g. McKenzie and Jackson, 1983, 1986; Dickinson, 1996). Although our geologic mapping did not yield evidence for clockwise rotation, paleomagnetic data show clockwise rotation in the eastern part of the Mina deflection (≥4-6°/Ma since the late Miocene to early Pliocene) (Petronis et al., 2009), to the west of the Mina deflection across the Bodie Hills region (~5°/Ma since the middle Miocene) (Rood et al., 2011) (Fig. 2B), and in the Adobe Hills region (15 ± 10° to 50 ± 10° since the Pliocene) (Grondin et al., 2016). Based on observations on the geometry, sinistral offset, and paired basins at the ends of active faults across the Mina deflection, Wesnousky (2005) also concluded that clockwise rotation of fault-bounded blocks characterized deformation in the Mina deflection. In addition, an elastic block model of GPS velocities across the Central Walker Lane showed vertical clockwise rotation of 2.0–2.5°/Ma for blocks bounded by sinistral faults within the Mina deflection and the Carson domain (Bormann et al., 2016) (Fig. 2B)[2].

Our kinematic models (Fig. 13) provide first order predictions for fault slip rates that are comparable to observations in the dextral and normal slip dominated northwestern part of the ECSZ, but the model does not match well our observations on fault slip rates in the sinistral slip dominated Mina deflection. Two possible explanations for this mismatch are (a) estimated minimum sinistral rates underestimate true rates and (b) that our model assumes irrotational deformation across Mina deflection which does not account for evidence of 5–60° of clockwise rotation across the Adobe Hills since the Pliocene (Grondin et al., 2016).

To account for clockwise rotation, and thus independently assess the magnitude of sinistral slip across the southwestern part of the Mina deflection, we apply Dickinson's (1996) trigonometric formulation for the pinned model, his preferred transrotation model, to the VBR region. In the pinned model, rotating blocks are pinned at their midlines to the edges of the shear zone, thus allowing the widths of the shear zone (W_o and W_n, before and after rotation) and rotating block (P_o and P_n, before and after rotation) to vary during transrotation while the length of the rotating block (L_c) remains fixed (Fig. 14). To calculate the magnitude of sinistral slip across the southwestern part of the Mina deflection, we first solve for the initial clockwise angle (ϕ) between the rotating block and shear zone boundaries using the following expressions derived for the pinned model (Dickinson, 1996) (Fig. 14) (Table 3).

$$\text{dextral slip} = S = W_n(\cos\phi - \cos\alpha) / \sin\alpha \quad (1)$$

where: α = post rotation clockwise angle between the rotating block and the shear zone boundary. We rearrange Equation (1) to solve for ϕ.

$$\phi = \arccos[(S^* \sin\alpha) / W_n) + \cos\alpha]. \quad (2)$$

[2]The GPS velocities of Bormann et al. (2016) take into account the postseismic viscoelastic relaxation following earthquakes in the Central Nevada Seismic belt, and relative to faults observed in the field, their block model simplifies the number and orientation of the faults bounding the blocks.

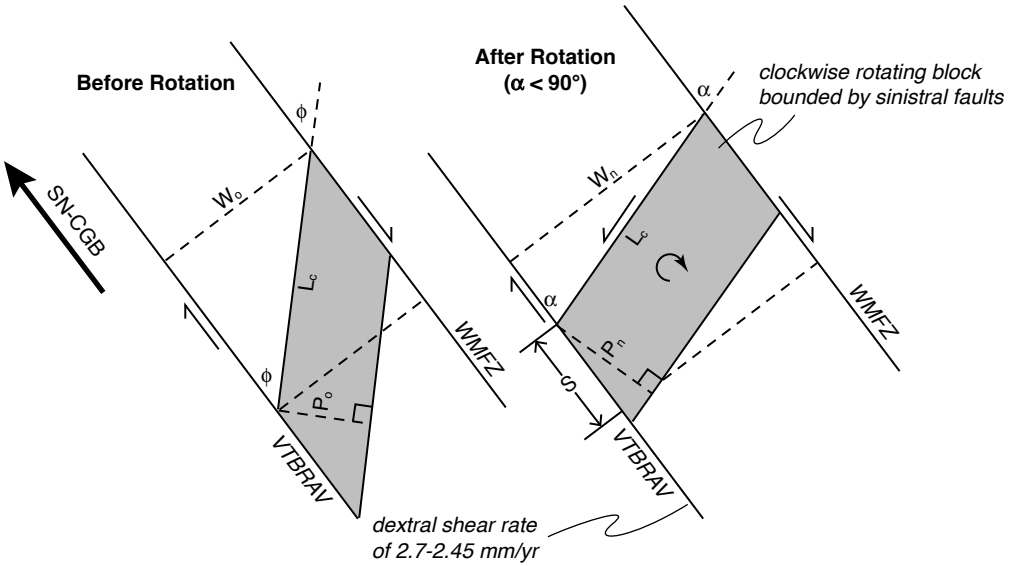

Figure 14. Pinned transrotation model showing clockwise rotating blocks (gray block), bounded by sinistral faults, within a zone of dextral shear across the northwestern eastern California shear zone and the southwestern Mina deflection, California-Nevada, USA. Heavy arrow shows the present-day azimuth of motion of the Sierra Nevada block with respect to the central Great Basin (SN-CGB) (Bennett et al., 2003). WMFZ—White Mountain fault zone; VTBRAV—Volcanic Tableland–Benton Range–Adobe Valley. Modified from Dickinson (1996).

Given a value for ϕ, we then calculate the magnitude of sinistral slip (R) using:

$$R = P_n(\cos\phi - \cos\alpha) / \sin\alpha. \quad (3)$$

We solved these equations for ϕ and R (Table 3) under the following simplifications and assumptions. We simplify the geometry of faulting such that the dextral shear zone is bounded by the White Mountains fault zone on the east and the faults that link the Volcanic Tableland–Benton Range–Adobe Valley on the west (cf. Figs. 13 and 14). To place this dextral shear zone in a Sierra Nevada–Central Great Basin relative motion reference frame, the map traces of the dextral faults bounding the zone in Figure 14 are parallel to 323° (the cardinal direction of the SN-CGB vector). The maximum width of this zone, Wn, is ~20 km (Fig. 13). We also simplify the sinistral fault bounded blocks in the southwest Mina deflection to a single rotating fault block (cf. Figs. 7A, 13, and 14). The width of the rotating fault block, Pn, from the Adobe Hills to the Coaldale fault is ~20 km (Fig. 13). In our kinematic model 1, all 2.8 mm/yr of dextral slip on the Owens Valley fault is partitioned onto the White Mountains fault zone and the Volcanic Tableland, and then transferred northward to the sinistral faults in the southwestern part of the Mina deflection (Fig. 13B). Decomposing the 2.8 mm/yr toward 323° yields a dextral shear rate of 2.7 mm/yr across our simplified dextral shear zone. A dextral shear rate of 2.7 mm/yr since 3.5 Ma to 3.0 Ma, bounds on the timing of fault slip across the southwestern Mina deflection, yields 9.5 km and 8.1 km of total dextral slip (S in Equation 1) (Table 3). In kinematic model 2, 2.8 mm/yr of dextral slip along the Owens Valley fault is partitioned into 1.9 mm/yr of dextral shear along the White Mountains fault zone, 0.3 mm/yr of dextral shear across the Volcanic Tableland, and 0.8 mm/yr of NW-dextral slip accommodated across the Coyote Warp onto the Round Valley fault. If this kinematic model configuration is correct, the 0.8 mm/yr of dextral slip appears to be transferred to the west of the Adobe Hills (Figs. 3 and 13C). Thus, in model 2, 2.5 mm/yr (parallel to 323°) is the net dextral shear rate across our simplified dextral shear zone that is transferred northward to the sinistral faults in the southwestern part of the Mina deflection (Figs. 13C and 14). A dextral shear rate of 2.5 mm/yr since 3.5 Ma to 3.0 Ma yields 8.6 km and 7.4 km of total dextral slip (S in Equation 1) (Table 3). Lastly, the average azimuth of sinistral faults across the southwestern Mina deflection changes from ~38° in the Adobe Hills to ~52° in the River Spring area. Thus, to estimate ϕ and sinistral slip R, we use α values of 75° for the Adobe Hills and 89° for the River Spring area (Table 3).

Solving Equations (2) and (3) for models 1 and 2, using both α values, yields sinistral slip rates that range from 2.1 to 3.2 mm/yr since 3.5 Ma to 3.0 Ma across the southwestern Mina deflection (Table 3). In contrast, the sum of documented sinistral geologic slip rates across the southwestern Mina deflection, from the Adobe Hills (Nagorsen-Rinke et al., 2013), River Spring area (this study), and the Coaldale fault (Bradley, 2005; Lee et al., 2006; Tincher and Stockli, 2009), yields a minimum geologic sinistral fault slip rate of ~1.4–1.8 mm/yr parallel to N50-60E. Our summed geologic sinistral slip rate is ~45%–85% of the transrotation predicted sinistral slip rate, suggesting that our minimum observed geologic sinistral slip rates underestimate the true geologic fault slip rates. In contrast, the transrotation model predicted sinistral slip rate

overlaps with the modeled geodetic sinistral shear rate of ~2.4 mm/yr (see next section). The overlap of geologic and geodetic rates suggests that the pinned model is a reasonable approximation for transrotation across this part of the Mina deflection, assuming no change in deformation rates over time. Finally, differencing our measured α angles and calculated ϕ angles yields the angle of rotation, ω, for the clockwise rotating block (Table 3). The angle of rotation ranges from 22° to 31°, well within the 5–60° clockwise rotation of Pliocene basalts in Adobe Hills reported by Grondin et al. (2016).

The quote "…all models are wrong, but some are useful" (Box and Draper, 1987) applies to our irrotational kinematic models (Fig. 13B and 13C) and transrotational model (Fig. 14). These models provide insight into the kinematics of fault slip transfer from the NW-striking dextral faults in the northwestern ECSZ onto NE-striking sinistral slip faults in the southwestern Mina deflection. However, these models cannot account for such geologic complexities as: (a) the variable magnitudes of vertical axis rotations across the Mina deflection (cf. Petronis et al., 2009; Rood et al., 2011; Bormann et al., 2016, Grondin et al., 2016), (b) the spatial and temporal distribution of vertical rotations, (c) the change in orientation of the rotating blocks and their bounding sinistral faults across the Mina deflection (cf. Wesnousky, 2005; Nagorsen-Rinke et al., 2013; this study), and (d) the range of potential block rotation mechanisms (e.g., variable versus constant shear zone widths; variable versus constant widths of rotating blocks; rotating blocks pinned at their ends versus middle).

TABLE 3. SOLUTIONS TO TRIGONOMETRIC EXPRESSIONS FOR DISPLACEMENTS AND ANGLES OF CLOCKWISE ROTATING BLOCKS WITHIN A DEXTRAL SHEAR ZONE, CALIFORNIA-NEVADA, USA

								Sinistral slip rate (mm/yr)	
Model	S	α	Wn	ϕ	ω	Pn	R	3.5 Ma	3.0 Ma
Model 1–Adobe Hills									
	9.5	75	20	44	31	20	9.5	2.7	3.2
	8.1	75	20	49	26	20	8.1	2.3	2.7
Model 2–Adobe Hills									
	8.6	75	20	48	27	20	8.6	2.5	2.9
	7.4	75	20	52	23	20	7.4	2.1	2.5
Model 1–River Spring									
	9.5	89	20	61	28	20	9.5	2.7	3.2
	8.1	89	20	65	24	20	8.1	2.3	2.7
Model 2–River Spring									
	8.6	89	20	63	26	20	8.6	2.5	2.9
	7.4	89	20	67	22	20	7.4	2.1	2.5

Notes: S—magnitude of dextral slip; α—post rotation clockwise angle between the rotating block and shear zone boundary; Wn—width of the shear zone after rotation; ϕ—initial clockwise angle between the rotating block and shear zone boundary; ω—clockwise rotation angle = α–ϕ; Pn—width of the rotating block after rotation; R—magnitude of sinistral slip.

Implications of GPS Velocities for Kinematic Models

Present-day strain accumulation across the Mina deflection from GPS velocities provides additional insight into our kinematic models. Bormann et al. (2016) developed an elastic block model of GPS velocities (see footnote 2) across the central Walker Lane Belt that yielded sinistral slip rates that sum to ~2.4 mm/yr along the average N45-60E–striking, sinistral faults that bound blocks in the southwestern Mina deflection from the northwestern side of the Excelsior Mountains to the Coaldale fault (Fig. 3). As noted in the previous section, the sum of observed sinistral geologic slip rates across the southwestern Mina deflection yields a minimum fault slip rate of ~1.4–1.8 mm/yr parallel to N50-60E. This geologic slip rate is ~58%–82% of the GPS derived rates. The difference between the geologic and GPS sinistral slip rates is probably the result of either documented minimum geologic slip rates that underestimate absolute slip rates, unaccounted for geologic slip on sinistral faults in the northern part of the Mina deflection, and/or our assumption of irrotational deformation is not valid. As shown above, applying a transrotation model to the transition from the northwestern ECSZ to the southwestern Mina deflection may eliminate the slip discrepancy. The transrotational model-derived geologic sinistral slip rate of 2.1–3.2 mm/yr overlaps the modeled GPS velocity of ~2.4 mm/yr of sinistral slip across this part of the Mina deflection (Bormann et al., 2016). Assuming that geologic slip rates have remained constant to the present-day, the similarity in transrotation predicted geologic sinistral slip rates and geodetic sinistral slip rates suggests that the absolute dextral slip rate along the Owens Valley fault is closer to Kirby et al.'s (2008) minimum estimate of 2.8 mm/yr, not the maximum of 4.5 mm/yr.

Geologic versus Geodetic Rates

Across the northern ECSZ at the latitude of ~36.5°N, summed geodetic strain rates (10^1 yrs) and geologic fault slip rates (10^3–10^6 yrs) calculated parallel to Pacific-North America plate motion (313°) (Dixon et al., 2000) are the same, within error, at ~9.3 mm/yr (cf. Bennett et al., 2003: Lee et al., 2009a) (Fig. 2B). In contrast, the modeled geodetic strain rate ~105 km to the north, within the northern ECSZ at ~37.5°N, is 10.6 ± 0.5 mm/yr (Lifton et al., 2013). This rate was calculated parallel to SN-CGB (323°) (Bennett et al., 2003) along a transect from the Sierra Nevada in the southwest to the San Antonio Mountains, Nevada (~38.25°/–117.10°) in the northeast (see line A-A′ in Fig. 3). This geodetic rate is ~370%–170% larger than the sum of the late Pleistocene geologic fault slip rates at ~3.0–5.9 mm/yr (Lifton et al., 2013 and references therein). The sum of geologic fault slip rates reported in Lifton et al. (2013) does not include several

geologic fault slip rates, including the approximately EW-extension across the Volcanic Tableland (Pinter, 1995; this study) and the Round Valley normal fault (Berry, 1997), NW-SE extension across the Lone Mountain fault (Lifton et al., 2015) and the faster dextral fault slip rates along the White Mountain fault zone (Lifton, 2013). These new or previously unconsidered slip rates may account for the apparent discrepancy between geologic and geodetic slip rates (e.g., Frankel et al., 2011; Nagorsen-Rinke et al., 2013).

To address this discrepancy, we compare Lifton et al.'s (2013) GPS rate of 10.6 ± 0.5 mm/yr toward 323°, calculated along a transect orthogonal to 323°, extending from the San Antonio Mountains, Nevada southwestward to the Sierra Nevada, California (see line A-A′ in Fig. 3), to the sum of published and new Pleistocene geologic fault slip rates along the same transect (Fig. 15; Table 4). For our geologic slip rate calculations, we compare the results using three different Pleistocene dextral fault slip rates along the White Mountain fault zone, a minimum 0.8 mm/yr (Kirby et al., 2006) (*v1*), a minimum 1.9 mm/yr (Lifton, 2013) (*v2*), and our kinematic model 1 predicted rate of 2.7 mm/yr (*v3*) (Fig. 15; Table 4). The sum of geologic fault slip rates parallel to 323° along this transect yields a dextral fault slip rate of 7.5 +1.2/–0.8 mm/yr (*v1*), 8.5 +1.3/–0.9 mm/yr (*v2*), and 9.3 +1.2/–0.8 mm/yr (*v3*), respectively. The first two summed geologic slip rates, *v1* and *v2*, are 60%–97% of the GPS rate, suggesting that most (all?) of the unaccounted for geologic slip is either along the White Mountain fault zone, along the ~NS-striking range front normal fault system that bounds the western flank of the San Antonio Mountains (fault No. 1340; https://earthquake.usgs.gov/hazards/qfaults/), and/or along the Round Valley fault (e.g., Phillips and Majkowski, 2011). One alternative explanation is that the GPS velocity is recording strain associated with fault slip (tectonic strain) *and* strain associated with magmatic processes (i.e., dike emplacement) (e.g., Bursik and Sieh, 1989; Smith et al., 2004), thus the discrepancy between GPS and geologic rates is not due to missing tectonic fault slip, but to additional magmatic strain. The other alternative explanation, that the GPS velocity is recording a strain transient and only tectonic strain, is problematic because such a transient would result in a strain compatibility problem with the ECSZ farther south where GPS and geologic slip rates match (c.f. Bennett et al., 2003; Lee et al., 2009a). In contrast, the third summed geologic slip rate, *v3*, is the same as the GPS rate, within error, if our predicted dextral slip rate of ~2.7 mm/yr along the White Mountain fault zone is correct, or if this NW-dextral shear rate is distributed across several faults, with most of it accommodated along the White Mountain fault zone.

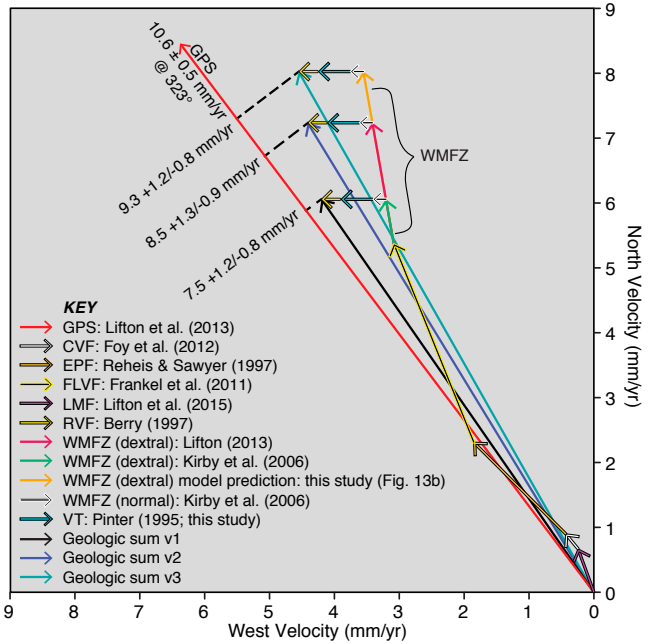

Figure 15. Velocity vector diagram comparing short-term (decadal) geodetic deformation rates versus long-term (Pleistocene; 10^3–10^5 yrs) geologic fault slip rates across the northern eastern California shear zone from the footwall to the Lone Mountain fault, Nevada in the northeast to the Sierra Nevada, California in the southwest, USA (see line A-A′ in Fig. 3). Three vectors are plotted for dextral slip along the White Mountain fault zone (WMFZ): a minimum slip rate of 0.8 mm/yr (Kirby et al., 2006), a minimum slip rate of 1.9 mm/yr (Lifton, 2013), and predicted slip rate of ~2.7 mm/yr from one of our kinematic models (see discussion in the text). The sum of the geologic fault slip rates is projected toward 323° (dashed lines), which is parallel to Sierra Nevada block relative to the central Great Basin (SN-CGB) motion. The GPS velocity of 10.6 ± 0.5 mm/yr is a model far field velocity of GPS vectors projected to line A-A′ (Fig. 3) (which is perpendicular to SN-CGB) and that takes into account interseismic strain (Lifton et al., 2013). Fault abbreviations not defined in Figures 2 or 3: CVF—Clayton Valley fault; EPF—Emigrant Peak fault; LMF—Lone Mountain fault; VT—Volcanic Tableland faults. Table 4 shows slip rates used in this diagram.

CONCLUSIONS

Our new geologic mapping, structural, and geochronologic data across the VBR region, which straddles the transition from the ECSZ to the Mina deflection, reveals a Miocene to Quaternary history of volcanism and deformation characterized by EW-extension, NW-dextral slip, and NE-sinistral slip. Based on these studies, we estimate new minimum Pliocene to Pleistocene extension, dextral, and sinistral fault slip rates for the VBR. Using our new fault slip rate estimates with published Pliocene to Pleistocene fault slip rates across other faults in the region (Stockli et al., 2000; Bradley, 2005; Kirby et al., 2006, 2008; Lee et al., 2006, 2009a; Tincher and Stockli, 2009; Nagorsen-Rinke et al., 2013), we propose two new irrotational kinematic fault slip models for the transition from the northwestern part of the ECSZ to the southwestern Mina deflection. Our two kinematic models show geologically plausible mechanisms for northward partitioning of dextral slip along the NNW-striking Owens Valley fault. Model 1 predicts partitioning of Owens Valley fault slip into two components, 2.7 mm/yr of dextral slip along the NW-striking White Mountain fault zone

TABLE 4. FAULT SLIP RATES USED IN SUMMATION OF LONG-TERM GEOLOGIC SLIP RATES ACROSS LATITUDE ~37.5°N, CALIFORNIA–NEVADA

Fault	Rate (mm/yr)	Time scale (ka)	Direction of slip (degrees)	Slip rate toward 323° (mm/yr)	Reference
CVF	0.3 ± 0.1	17	320	0.3 ± 0.1	Foy et al. (2012)
EPF	2.0 +0.9/–0.8[†]	5–8	315	2.0 +0.9/–0.8	Reheis and Sawyer (1997)
FLVFC	3.3 +0.7/–0.1	71	338	3.2 +0.7/–0.1	Frankel et al. (2011)
LMF	0.7 ± 0.1	8	340	0.7 ± 0.1	Lifton et al. (2015)
RVF	0.3 ± 0.1[ε]	15–25	270	0.2 ± 0.1	Berry (1997)
WMFZ (v1)	0.7–0.8	766	350	0.7 ± 0.1	Kirby et al. (2006)
WMFZ (v2)	1.9 +0.5/–0.4	38	350	1.7 +0.5/–0.4	Lifton (2013)
WMFZ (v3)	2.7	—	350	2.4	This study
WMFZ (normal)	0.2 ± 0.1[§]	766	270	0.1 ± 0.1	Kirby et al. (2006)
VT	0.5 +0.2/–0.1	766	270	0.3 +0.2/–0.1	This study
Sum of fault slip rates					
v1				7.5 +1.2/–0.8	
v2				8.5 +1.3/–0.9	
v3				9.3 +1.2/–0.8	

[†]Horizontal extension rate is based on the preferred vertical slip rate of Reheis and Sawyer (1997) and a range in normal fault dip of 50–70°.
[ε]Horizontal extension rate is based on Berry's (1997) measured range in surface offset across fault scarps, estimated age of offset landform, and assuming a range in normal fault dip of 50–70°.
[§]Based on 160 ± 40 m extension to 270° since eruption of the Bishop Tuff, California.
CVF—Clayton Valley fault; EPF—Emigrant Peak fault; FLVFC—Fish Lake Valley–Furnace Creek fault zone; LMF—Lone Mountain fault; RVF—Round Valley fault; WMFZ—White Mountain fault zone; VT—Volcanic Tableland faults.

and 0.5 mm/yr of EW-extension across the Volcanic Tableland. Model 2 predicts partitioning of Owens Valley fault slip into three components, 1.9 mm/yr of dextral slip along the White Mountain fault zone, 0.5 mm/yr of extension across the Volcanic Tableland, and 0.8 mm/yr of NNW-dextral slip across the Coyote Warp and onto the Sierra Nevada range front fault. However, farther to the north across the NW-striking dextral and NE-striking sinistral faults that define the boundary between the ECSZ and Mina deflection, both of our idealized kinematic models yield predicted fault slip rates that are larger than our measured minimum rates. The difference between observations and model predictions is best explained by minimum calculated slip rate estimates that underestimate absolute rates. The invalidity of one or more of our other assumptions that underlie our simplified irrotational kinematic models may also be contributing factors. Applying a simple transrotation model to the ECSZ-Mina deflection transition suggests that sinistral slip rates across the southwestern Mina deflection should be at least 115% greater than the minimum geologic slip rate we documented.

Summing our new geologic fault slip rates with recently published or previously unconsidered slip rates, parallel to motion of SN-CGB, from the Sierra Nevada northeastward into western Nevada yields a minimum geologic slip rate of 9.3 +0.8/–0.2 mm/yr. This minimum rate is the same, within error, as the geodetic rate along the same transect, if our assumption that the geologic slip rate along the dextral White Mountain fault zone is ~2.7 mm/yr.

The geometry and style of faults we document across the transition from the northern ECSZ into the southwestern Mina deflection, combined with published geologic mapping and paleomagnetic studies elsewhere in the Mina deflection, indicate that the Mina deflection defines a clockwise right-stepping rotational stepover within the ECSZ-WLB dextral shear zone. This rotational stepover is characterized by rotating blocks and bounding sinistral faults that change orientation and size along their length creating a far more complicated stepover geometry than defined in simple kinematic models.

ACKNOWLEDGMENTS

Thanks to Jacob Bradley, Gabe Creason, Peter Dubyoski, and Tucker Lance for their excellent assistance and company during field work, and to R. Allmendinger for developing the stereonet program we used in Figure 10. Discussions about the geology and GPS data with C. Henry and Z. Lifton were helpful. Thorough and constructive comments from two anonymous reviewers and from AE T. Pavlis are much appreciated for improving the clarity of our data descriptions and interpretations. Funding for this research was supported by U.S. Geological Survey National Cooperative Geologic Mapping Program Grants G13AC00123 and G14AC00161 awarded to JL. KD received additional funding from Central Washington University, the Geological Society of America, the Northern California Geological Society, the West Seattle Rock Club (Northwest Federation of Mineralogical Societies), and University of California White Mountain Research Center. RR received additional funding from the Geological Society of America, Sigma Xi, and University of California White Mountain Research Center. Any use of trade, firm, or product names is for descriptive purposes only and does not imply endorsement by the U.S. Government. The views and conclusions contained in this document are those of the authors and should not be

interpreted as necessarily representing the official policies, either expressed or implied, of the U.S. Government.

REFERENCES CITED

Aydin, A., and Nur, A., 1982, Evolution of pull-apart basins and their scale independence: Tectonics, v. 1, p. 91–105, https://doi.org/10.1029/TC001i001p00091.

Bailey, R.A., Dalrymple, G.B., and Lanphere, M.A., 1976, Volcanism, structure, and geochronology of Long Valley Caldera, Mono County, California: Journal of Geophysical Research. Solid Earth and Planets, v. 81, no. 5, p. 725–744, https://doi.org/10.1029/JB081i005p00725.

Bartley, J.M., Glazner, A.F., Coleman, D.S., Kylander-Clark, A., Mapes, R., and Friedrich, A.M., 2007, Large Laramide dextral offset across Owens Valley, California, and its possible relation to tectonic unroofing of the southern Sierra Nevada, *in* Roeske, S.M., Till, A.B., Foster, D.A., and Sample, J.C., eds., Exhumation Associated with Continental Strike-Slip Fault Systems: Geological Society of America Special Paper 434, p. 129–148, https://doi.org/10.1130/2007.2434(07).

Bateman, P.C., 1965, Geology and tungsten mineralization of the Bishop district, California, with a section on gravity study of Owens Valley and a section on seismic profile: U.S. Geological Survey Professional Paper 470, 208 p., https://doi.org/10.3133/pp470.

Bennett, R., Wernicke, B., Niemi, N.A., Friedrich, A.M., and Davis, J.L., 2003, Contemporary strain rates in the northern Basin and Range Province from GPS data: Tectonics, v. 22, no. 2, https://doi.org/10.1029/2001TC001355.

Berry, M.E., 1997, Geomorphic analysis of late Quaternary faulting on Hilton Creek, Round Valley and Coyote warp faults, east-central Sierra Nevada, California, USA: Geomorphology, v. 20, p. 177–195, https://doi.org/10.1016/S0169-555X(97)00033-0.

Bormann, J.M., Hammond, W.C., Kreemer, C., and Blewitt, G., 2016, Accommodation of missing shear strain in the Central Walker Lane, western North America: Constraints from dense GPS measurements: Earth and Planetary Science Letters, v. 440, p. 169–177, https://doi.org/10.1016/j.epsl.2016.01.015.

Box, G.E.P., and Draper, N.R., 1987, Empirical Model-Building and Response Surfaces, Wiley Series in Probability and Mathematical Statistics: Hoboken, New Jersey, John Wiley & Sons, 688 p.

Bradley, D., 2005, The Kinematic History of the Coaldale Fault, Walker Lane Belt, Nevada [M.S. thesis]: Lawrence, Kansas, University of Kansas, 96 p.

Bursik, M., and Sieh, K., 1989, Range front faulting and volcanism in the Mono Basin, eastern California: Journal of Geophysical Research. Solid Earth, v. 94, p. 15,587–15,609, https://doi.org/10.1029/JB094iB11p15587.

Cashman, P.H., and Fontaine, S.A., 2000, Strain partitioning in the northern Walker Lane, western Nevada and northeastern California: Tectonophysics, v. 326, p. 111–130, https://doi.org/10.1016/S0040-1951(00)00149-9.

Casteel, J.C., 2005, Late Miocene to Holocene faulting along the southwestern Inyo Mountains fault zone, eastern California, [M.S. thesis]: Ellensburg, Washington, Central Washington University, 72 p.

Chamberlain, K.J., Wilson, C.J.N., Wooden, J.L., Charlier, B.L.A., and Ireland, T.R., 2014, New perspectives on the Bishop Tuff from zircon textures, ages and trace elements: Journal of Petrology, v. 55, no. 2, p. 395–426, https://doi.org/10.1093/petrology/egt072.

Christie-Blick, N., and Biddle, K.T., 1985, Deformation and basin formation along strike-slip faults, *in* Biddle, K.T., and Christie-Blick, N., eds., Strike-Slip Deformation, Basin Formation, and Sedimentation: Tulsa, Oklahoma, Society of Economic Paleontologists and Mineralogists Special Publication 37, p. 1–34, https://doi.org/10.2110/pec.85.37.0001.

Crowder, D.F., and Sheridan, M.F., 1972, Geologic map of the White Mountain Peak quadrangle, Mono County, California: U.S. Geological Survey Geologic Quadrangle Map 1012, scale 1:62,500, https://doi.org/10.3133/gq1012.

Crowder, D.F., Robinson, P.T., and Harris, D.L., 1972, Geologic Map of the Benton Quadrangle, Mono County, California and Esmeralda and Mineral Counties, Nevada: U.S. Geological Survey Geologic Quadrangle Map 1013, scale 1:62,500, https://doi.org/10.3133/gq1013.

Crowell, J.C., 1974, Origin of late Cenozoic basins of southern California, *in* Dickinson, W.R., ed., Tectonics and Sedimentation: Tulsa, Oklahoma, Society of Economic Paleontologists and Mineralogists Special Publication 22, p. 190–204, https://doi.org/10.2110/pec.74.22.0190.

Cunningham, W.D., and Mann, P., 2007, Tectonics of strike-slip restraining and releasing bends, *in* Cunningham, W.D., and Mann, P., eds., Tectonics of Strike-Slip Restraining and Releasing Bends: Geological Society of London Special Publication 290, p. 1–12, https://doi.org/10.1144/SP290.1.

Dickinson, W.R., 1996, Kinematics of Transrotational Tectonism in the California Transverse Ranges and Its Contribution to Cumulative Slip Along the San Andres Transform Fault System: Geological Society of America Special Paper 305, 46 p., https://doi.org/10.1130/0-8137-2305-1.1.

Dilles, J.H., and Gans, P.B., 1995, The chronology of Cenozoic volcanism and deformation in the Yerington area, western Basin and Range and Walker Lane: Geological Society of America Bulletin, v. 107, no. 4, p. 474–486, https://doi.org/10.1130/0016-7606(1995)107<0474:TCOCVA>2.3.CO;2.

Dixon, T.H., Robaudo, S., Lee, J., and Reheis, M.C., 1995, Constraints on present-day Basin and Range deformation from space geodesy: Tectonics, v. 14, no. 4, p. 755–772, https://doi.org/10.1029/95TC00931.

Dixon, T.H., Miller, M., Farina, F., Wang, H., and Johnson, D., 2000, Present-day motion of the Sierra Nevada block and some tectonic implications for the Basin and Range province, North American Cordillera: Tectonics, v. 19, no. 1, p. 1–24, https://doi.org/10.1029/1998TC001088.

Dokka, R.K., and Travis, C.J., 1990, Late Cenozoic strike-slip faulting in the Mojave Desert, California: Tectonics, v. 9, p. 311–340, https://doi.org/10.1029/TC009i002p00311.

Dubyoski, P., Lee, J., and Calvert, A., 2016, Tuff-filled paleovalleys dextrally offset across the Benton Springs fault, central Walker Lane, Nevada: Geological Society of America Abstracts with Programs, v. 48, https://doi.org/10.1130/abs/2016AM-283180.

Faulds, J.E., and Henry, C.D., 2008, Tectonic influences on the spatial and temporal evolution of the Walker Lane: An incipient transform fault along the evolving Pacific–North American plate boundary, *in* Spencer, J.E., and Titley, S.R., eds., Ores and Orogenesis: Circum-Pacific Tectonics, Geologic Evolution, and Ore Deposits: Arizona Geological Society Digest 22, p. 437-470.

Fleck, R.J., and Calvert, A.T., 2016, Intercalibration of $^{40}Ar/^{39}Ar$ mineral standards with Bodie Hills sanidine: Geological Society of America Abstracts with Programs, v. 48, https://doi.org/10.1130/abs/2016AM-286011.

Foy, T.A., Frankel, K.L., Lifton, Z.M., Johnson, C.W., and Caffee, M.W., 2012, Distributed extensional deformation in a zone of right-lateral shear: Implications for geodetic versus geologic rates of deformation in the eastern California shear zone-Walker Lane: Tectonics, v. 31, no. 4, https://doi.org/10.1029/2011TC002930.

Frankel, K.L., Dolan, J.F., Finkel, R.C., Owen, L.A., and Hoeft, J.S., 2007, Spatial variations in slip rate along the Death Valley-Fish Lake Valley fault system determined from LiDAR topographic data and cosmogenic ^{10}Be geochronology: Geophysical Research Letters, v. 34, no. 18, https://doi.org/10.1029/2007GL030549.

Frankel, K.L., Dolan, J.F., Owen, L.A., Ganev, P., and Finkel, R.C., 2011, Spatial and temporal constancy of seismic strain release along an evolving segment of the Pacific-North America plate boundary: Earth and Planetary Science Letters, v. 304, no. 3–4, p. 565–576, https://doi.org/10.1016/j.epsl.2011.02.034.

Gamond, J., 1987, Bridge structures as sense of displacement criteria in brittle fault zones: Journal of Structural Geology, v. 9, p. 609–620, https://doi.org/10.1016/0191-8141(87)90146-5.

Gilbert, C.M., 1938, Welded tuff in eastern California: Geological Society of America Bulletin, v. 49, p. 1829–1862, https://doi.org/10.1130/GSAB-49-1829.

Gilbert, C.M., Christensen, M.N., Yehya Al-Rawl, and Lajoie, K.R., 1968, Structural and volcanic history of Mono Basin, California-Nevada, *in* Coats, R.R., Hay, R.L., and Anderson, C.A., eds., Studies in Volcanology: Geological Society of America Memoir 116, p. 275–329.

Grondin, D.P., Petronis, M., Lindline, J., and Romero, B.P., 2016, Vertical axis clockwise rotation of fault blocks in the eastern Mono Basin, California and Nevada: Geological Society of America Abstracts with Programs, v. 48, https://doi.org/10.1130/abs/2016AM-286303.

Higgins, C.T., Flynn, T., Chapman, R.H., Trexler, D.T., Chase, G.R., Bacon, C.F., and Ghusn, G., Jr., 1985, Geothermal systems of the Mono Basin-Long Valley region, eastern California and western Nevada: California Division of Mines and Geology, Open-File Report 85-19, 159 p., 9 plates.

Hoeft, J.S., and Frankel, K.L., 2010, Temporal variations in extension rate on the Lone Mountain fault and strain distribution in the eastern California shear zone-Walker Lane: Geosphere, v. 6, p. 917–936, https://doi.org/10.1130/GES00603.1.

Hogan, E., 2014, Structural deformation across the southwest Mina deflection, California-Nevada: Field studies in the Huntoon Springs Quadrangle [M.S. thesis]: Ellensburg, Washington, Central Washington University.

Hoxey, A., Lee, J., and Calvert, A., 2018, Spatial and temporal characterization of volcanic-filled paleovalleys dextrally offset across the Petrified Springs fault in the central Walker Lane, Nevada: Geological Society of America Abstracts with Programs. v. 50, https://doi.org/10.1130/abs/2018RM-313525.

Ingersoll, R.V., 1988, Tectonics of sedimentary basins: Geological Society of America Bulletin, v. 100, p. 1704–1719, https://doi.org/10.1130/0016-7606(1988)100<1704:TOSB>2.3.CO;2.

Kirby, E., Burbank, D.W., Reheis, M., and Phillips, F., 2006, Temporal variations in slip rate of the White Mountain fault zone, Eastern California: Earth and Planetary Science Letters, v. 248, no. 1–2, p. 168–185, https://doi.org/10.1016/j.epsl.2006.05.026.

Kirby, E., Anandakrishnan, S., Phillips, F., and Marrero, S., 2008, Late Pleistocene slip rate along the Owens Valley fault, eastern California: Geophysical Research Letters, v. 35, no. 1, https://doi.org/10.1029/2007GL031970.

Krauskopf, K.B., and Bateman, P.C., 1977, Geologic map of the Glass Mountain Quadrangle, Mono County, California, and Mineral County, Nevada: U.S. Geological Survey Geologic Quadrangle Map 1099, scale 1:62,500.

Kuiper, K.F., Deino, A., Hilgen, F.J., Krijgsman, W., Renne, P.R., and Wijbrans, J.R., 2008, Synchronizing rock clocks of Earth History: Science, v. 320, p. 500–504, https://doi.org/10.1126/science.1154339.

Larsen, N.W., 1979, Chronology of late Cenozoic basaltic volcanism: The tectonic implications along a segment of the Sierra Nevada and Basin and Range Province boundary [Ph.D. thesis]: Provo, Utah, Brigham Young University, 95 p.

Lee, J., Rubin, C.M., and Calvert, A., 2001, Quaternary faulting history along Deep Springs fault, California: Geological Society of America Bulletin, v. 113, p. 855–869, https://doi.org/10.1130/0016-7606(2001)113<3C0855:QFHATD>3E2.0.CO;2.

Lee, J., Stockli, D., Schroeder, J., Tincher, C., Bradley, D., Owen, L., Gosse, J., Finkel, R., and Garwood, J., 2006, Fault Slip Transfer in the Eastern California Shear Zone-Walker Lane Belt: Geological Society of America Penrose Conference Field Trip Guide, 26 p., https://doi.org/10.1130/2006.FSTITE.PFG.

Lee, J., Stockli, D.F., Owen, L.A., Finkel, R.C., and Kislitsyn, R., 2009a, Exhumation of the Inyo Mountains, California: Implications for the timing of extension along the western boundary of the Basin and Range Province and distribution of dextral fault slip rates across the eastern California shear zone: Tectonics, v. 28, https://doi.org/10.1029/2008TC002295.

Lee, J., Garwood, J., Stockli, D.F., and Gosse, J., 2009b, Quaternary faulting in Queen Valley, California-Nevada: Implications for kinematics of fault-slip transfer in the eastern California shear zone-Walker Lane belt: Geological Society of America Bulletin, v. 121, no. 3–4, p. 599–614, https://doi.org/10.1130/B26352.1.

Lienkaemper, J.J., Pezzopane, S.K., Clark, M.M., and Rymer, M.J., 1987, Fault fractures formed in association with the 1986 Chalfant Valley, California, earthquake sequence: Preliminary report: Bulletin of the Seismological Society of America, v. 77, no. 1, p. 297–305.

Lifton, Z.M., 2013, Understanding an evolving diffuse plate boundary with geodesy and geochronology [Ph.D. thesis]: Atlanta, Georgia, Georgia Institute of Technology, 108 p.

Lifton, Z.M., Newman, A.V., Frankel, K.L., Johnson, C.W., and Dixon, T.H., 2013, Insights into distributed plate rates across the Walker Lane from GPS geodesy: Geophysical Research Letters, v. 40, p. 4620–4624, https://doi.org/10.1002/grl.50804.

Lifton, Z.M., Frankel, K.L., and Newman, A.V., 2015, Latest Pleistocene and Holocene slip rates on the Lone Mountain fault: Evidence for accelerating slip in the Silver Peak-Lone Mountain extensional complex: Tectonics, v. 34, no. 3, p. 449–463, https://doi.org/10.1002/2013TC003512.

Mayberry, C., and Lee, J., 2017, Geologic mapping along the Gumdrop Hills fault: Dextrally offset tuff-filled paleovalleys in the Central Walker Lane: Geological Society of America Abstracts with Programs, v. 49, no. 6, https://doi.org/10.1130/abs/2017AM-308732.

McKenzie, D., and Jackson, J., 1983, The relationship between strain rates, crustal thickening, paleomagnetism, finite strain and fault movements within a deforming area: Earth and Planetary Science Letters, v. 65, p. 182–202, https://doi.org/10.1016/0012-821X(83)90198-X.

McKenzie, D., and Jackson, J., 1986, A block model of distributed deformation by faulting: Journal of the Geological Society, London, v. 143, p. 349–353, https://doi.org/10.1144/gsjgs.143.2.0349.

Metz, J.M., and Mahood, G.A., 1985, Precursors to the Bishop Tuff Eruption: Glass Mountain, Long Valley, California: Journal of Geophysical Research. Solid Earth, v. 90, p. 11121–11126, https://doi.org/10.1029/JB090iB13p11121.

Nagorsen-Rinke, S., Lee, J., and Calvert, A., 2013, Pliocene sinistral slip across the Adobe Hills, eastern California-western Nevada: Kinematics of fault slip transfer across the Mina deflection: Geosphere, v. 9, no. 1, p. 37–53, https://doi.org/10.1130/GES00825.1.

Oldow, J.S., 1992, Late Cenozoic displacement partitioning in the northwestern Great Basin, *in* Lane, C., and Steven, D., eds., Geological Society of Nevada Walker Lane Symposium: Structure, Tectonics and Mineralization of the Walker Lane: Reno, Nevada, Geological Society of Nevada, p. 17–52.

Oldow, J.S., 2003, Active transtensional boundary zone between the western Great Basin and Sierra Nevada block, western U.S. Cordillera: Geology, v. 31, p. 1033–1036, https://doi.org/10.1130/G19838.1.

Oldow, J.S., Bally, A.W., Lallemant, H.G.A., and Leeman, W.P., 1989, Phanerozoic evolution of the North American Cordillera; United States and Canada, *in* Bally, A.W., and Palmer, A.R., eds., An Overview: Boulder, Colorado, Geological Society of America, Geology of North America, v. A, p. 139–232, https://doi.org/10.1130/DNAG-GNA-A.139.

Oldow, J.S., Kohler, G., and Donelick, R.A., 1994, Late Cenozoic extensional transfer in the Walker Lane strike-slip belt, Nevada: Geology, v. 22, p. 637–640, https://doi.org/10.1130/0091-7613(1994)022<0637:LCETIT>2.3.CO;2.

Oldow, J.S., Elias, E.A., Ferranti, L., McClelland, W.C., and McIntosh, W.C., 2009, Late Miocene to Pliocene synextensional deposition in fault-bounded basins within the upper plate of the western Silver Peak-Lone Mountain extensional complex, west-central Nevada, *in* Oldow, J.S., and Cashman, P.H., eds., Late Cenozoic Structure and Evolution of the Great Basin-Sierra Nevada Transition: Geological Society of America Special Paper 447, p. 275–312, https://doi.org/10.1130/2009.2447(14).

Oskin, M., Perg, L., Blumentritt, D., Mukhopadhyay, S., and Iriondo, A., 2007, Slip rate of the Calico fault: Implications for geologic versus geodetic rate discrepancy in the Eastern California Shear Zone: Journal of Geophysical Research. Solid Earth, v. 112, no. B2, https://doi.org/10.1029/2006JB004451.

Peltzer, G., Crampe, F., Hensley, S., and Rosen, P., 2001, Transient strain accumulation and fault interaction in the Eastern California shear zone: Geology, v. 29, p. 975–978, https://doi.org/10.1130/0091-7613(2001)029<0975:TSAAFI>2.0.CO;2.

Pérouse, E., and Wernicke, B.P., 2016, Spatialtemporal evolution of fault slip rates in deforming continents: The case of the Great Basin region, northern Basin and Range province: Geosphere, v. 13, p. 112–135, https://doi.org/10.1130/GES01295.1.

Petronis, M.S., Geissman, J.W., Oldow, J.S., and McIntosh, W.C., 2009, Late Miocene to Pliocene vertical-axis rotation attending development of the Silver Peak-Lone Mountain displacement transfer zone, west-central Nevada, *in* Oldow, J.S., and Cashman, P.H., eds., Late Cenozoic Structure and Evolution of the Great Basin-Sierra Nevada Transition: Geological Society of America Special Paper 447, p. 215–253, https://doi.org/10.1130/2009.2447(12).

Phillips, F.M., and Majkowski, L., 2011, The role of low-angle normal faulting in active tectonics of the northern Owens Valley, California: Lithosphere, v. 3, p. 22–36, https://doi.org/10.1130/L73.1.

Pinter, N., 1995, Faulting on the volcanic tableland, Owens Valley, California: The Journal of Geology, v. 103, p. 73–83, https://doi.org/10.1086/629723.

Reheis, M.C., and Sawyer, T.L., 1997, Late Cenozoic history and slip rates of the Fish Lake Valley, Emigrant Peak, and Deep Springs fault zones, Nevada and California: Geological Society of America Bulletin, v. 109, p. 280–299, https://doi.org/10.1130/0016-7606(1997)109<0280:LCHASR>2.3.CO;2.

Reheis, M.C., Stine, S., and Sarna-Wojcicki, A.M., 2002, Drainage reversals in Mono Basin during the late Pliocene and Pleistocene: Geological Society of America Bulletin, v. 114, no. 8, p. 991–1006, https://doi.org/10.1130/0016-7606(2002)114<0991:DRIMBD>2.0.CO;2.

Rinehart, C.D., and Ross, D.C., 1957, Geologic map of the Casa Diablo Mountain quadrangle, California: U.S. Geological Survey Geologic Quadrangle Map 99, scale 1:62,500.

Rockwell, T.K., Lindvall, S., Herzberg, M., Murbach, D., Dawson, T., and Berger, G., 2000, Paleoseismology of the Johnson Valley, Kickapoo, and Homestead Valley faults: Clustering of earthquakes in the eastern California shear zone: Bulletin of the Seismological Society of America, v. 90, p. 1200–1236, https://doi.org/10.1785/0119990023.

Rood, D.H., Burbank, D.W., Herman, S.W., and Bogue, S., 2011, Rates and timing of vertical-axis block rotations across the central Sierra Nevada-Walker Lane transition in the Bodie Hills, California/Nevada: Tectonics, v. 30, no. 5, https://doi.org/10.1029/2010TC002754.

Sheehan, T.P., 2007, Evolution of Neogene Fault Populations in northern Owens Valley, California and Implications for the Eastern California Shear Zone [Ph.D. thesis]: New Orleans, Louisiana, Tulane University, 207 p.

Smith, K.D., and Priestley, K.F., 2000, Faulting in the 1986 Chalfant, California, Sequence: Local Tectonics and Earthquake Source Parameters: Bulletin of the Seismological Society of America, v. 90, no. 4, p. 813–831, https://doi.org/10.1785/0119990129.

Smith, K.D., von Seggern, D., Blewitt, G., Preston, L., Anderson, J.G., Wernicke, B.P., and Davis, J.L., 2004, Evidence for deep magma injection beneath Lake Tahoe, Nevada-California: Science, v. 305, p. 1277–1280, https://doi.org/10.1126/science.1101304.

Sternlof, K.R., 1988, Structural style and kinematic history of the active Panamint-Saline extensional system, Inyo County, California, [M.S. thesis]: Cambridge, Massachusetts, Massachusetts Institute of Technology, 40 p.

Stockli, D.F., Farley, K.A., and Dumitru, T.A., 2000, Calibration of the apatite (U-Th)/He thermochronometer on an exhumed fault block, White Mountains, California: Geology, v. 28, p. 983–986, https://doi.org/10.1130/0091-7613(2000)28<983:COTAHT>2.0.CO;2.

Stockli, D.F., Surpless, B.E., and Dumitru, T.A., 2002, Thermochronological constraints on the timing and magnitude of Miocene and Pliocene extension in the central Wassuk Range, western Nevada: Tectonics, v. 21, 1028, https://doi.org/10.1029/2001TC001295.

Stockli, D.F., Dumitru, T.A., McWilliams, M.O., and Farley, K.A., 2003, Cenozoic tectonic evolution of the White Mountains, California and Nevada: Geological Society of America Bulletin, v. 115, no. 7, p. 788–816, https://doi.org/10.1130/0016-7606(2003)115<0788:CTEOTW>2.0.CO;2.

Surpless, B.E., Stockli, D.F., Dumitru, T.A., and Miller, E.L., 2002, Two-phase westward encroachment of Basin and Range extension into the northern Sierra Nevada: Tectonics, v. 21, https://doi.org/10.1029/2000TC001257.

Taylor, G.F., 1934, Scarp ramp in northern Owens Valley [abstract]: Proceedings of the Geological Society of America, v. 1933, p. 309.

Tincher, C.R., and Stockli, D.F., 2009, Cenozoic Volcanism and Tectonics in the Queen Valley Area, Esmeralda County, Western Nevada, *in* Oldow, J.S., and Cashman, P.H., eds., Late Cenozoic Structure and Evolution of the Great Basin-Sierra Nevada Transition: Geological Society of America Special Paper 447, p. 255–274, https://doi.org/10.1130/2009.2447(13).

Tosdal, R.M., Wooden, J.L., and Kistler, R.W., 2000, Geometry of the Neoproterozoic continental break-up, and implications for location of Nevadan mineral belts, *in* Cluer, J.K., Price, J.G., Struhsacker, E.M., Hardyman, R.F., and Morris, C.L., eds., Geology and Ore Deposits 2000: The Great Basin and Beyond: Geological Society of Nevada Symposium Proceedings, May 15–18, p. 451–466.

Unruh, J., Humphrey, J., and Barron, A., 2003, Transtensional model for the Sierra Nevada frontal fault system, eastern California: Geology, v. 31, no. 4, p. 327–330, https://doi.org/10.1130/0091-7613(2003)031<0327:TMFTSN>2.0.CO;2.

Wesnousky, S.G., 2005, Active faulting in the Walker Lane: Tectonics, v. 24, https://doi.org/10.1029/2004TC001645.

Wesnousky, S.G., and Jones, C.H., 1994, Oblique slip, slip partitioning, spatial and temporal changes in the regional stress field, and the relative strength of active faults in the Basin and Range, western United States: Geology, v. 22, p. 1031–1034, https://doi.org/10.1130/0091-7613(1994)022<1031:OSSPSA>2.3.CO;2.

Wilcox, R.E., Harding, T.P., and Seely, D.R., 1973, Basic wrench tectonics: AAPG Bulletin, v. 57, p. 74–96.